J. Fluid Mech. (2010), *vol.* 656, *pp.* 417–447. © Cambridge University Press 2010
doi:10.1017/S0022112010001242

On the stability of plane Couette–Poiseuille flow with uniform crossflow

ANIRBAN GUHA[1,2]† AND IAN A. FRIGAARD[3,4]

[1]Institute of Applied Mathematics, University of British Columbia, 6356 Agricultural Road, Vancouver, BC, V6T 1Z2, Canada

[2]Department of Civil Engineering, University of British Columbia, 2002-6250 Applied Science Lane, Vancouver, BC, V6T 1Z4, Canada

[3]Department of Mathematics, University of British Columbia, 1984 Mathematics Road, Vancouver, BC, V6T 1Z2, Canada

[4]Department of Mechanical Engineering, University of British Columbia, 2054-6250 Applied Science Lane, Vancouver, BC, V6T 1Z4, Canada

(Received 3 October 2009; revised 7 March 2010; accepted 8 March 2010;
first published online 2 June 2010)

We present a detailed study of the linear stability of the plane Couette–Poiseuille flow in the presence of a crossflow. The base flow is characterized by the crossflow Reynolds number R_{inj} and the dimensionless wall velocity k. Squire's transformation may be applied to the linear stability equations and we therefore consider two-dimensional (spanwise-independent) perturbations. Corresponding to each dimensionless wall velocity, $k \in [0, 1]$, two ranges of R_{inj} exist where unconditional stability is observed. In the lower range of R_{inj}, for modest k we have a stabilization of long wavelengths leading to a cutoff R_{inj}. This lower cutoff results from skewing of the velocity profile away from a Poiseuille profile, shifting of the critical layers and the gradual decrease of energy production. Crossflow stabilization and Couette stabilization appear to act via very similar mechanisms in this range, leading to the potential for a robust compensatory design of flow stabilization using either mechanism. As R_{inj} is increased, we see first destabilization and then stabilization at very large R_{inj}. The instability is again a long-wavelength mechanism. An analysis of the eigenspectrum suggests the cause of instability is due to resonant interactions of Tollmien–Schlichting waves. A linear energy analysis reveals that in this range the Reynolds stress becomes amplified, the critical layer is irrelevant and viscous dissipation is completely dominated by the energy production/negation, which approximately balances at criticality. The stabilization at very large R_{inj} appears to be due to decay in energy production, which diminishes like R_{inj}^{-1}. Our study is limited to two-dimensional, spanwise-independent perturbations.

1. Introduction

From the perspective of applications in technology, Poiseuille flow of viscous fluid along a duct is undoubtedly one of the most important flows studied as it underpins the field of hydraulics. Instability and subsequent transition from laminar flow marks a paradigm shift in the dominant transport mechanisms of mass, momentum and heat, and it is for this reason that the subject remains of enduring interest, even after

---

† Email address for correspondence: aguha@interchange.ubc.ca

more than 100 years of study. In this paper, we focus on two methods for affecting the linear stability of plane Poiseuille (PP) flow. The first method consists of introducing a Couette component to the flow, by translation of one of the walls. The second method consists of introducing a crossflow, e.g. via injection through a porous wall. While both effects have been studied individually to some extent, there are fewer studies of the two effects combined, which is the main focus here.

We first summarize the effects of a Couette component on a plane Poiseuille flow. The main curiosity here stems from the observation that PP flow is linearly unstable when the critical Reynolds number exceeds $R_c \approx 5772$ (Reynolds number based on the centreline axial velocity and the half-width of the channel; see Orszag 1971), whereas the plane Couette (PC) flow is absolutely stable with respect to infinitesimal amplitude disturbances, $R_c = \infty$; see Romanov (1973). Superimposing PP and PC flows, we may ask if a small Couette component can affect the stability of the PP flow. The stability of plane Couette–Poiseuille (PCP) flow was first studied by Potter (1966) and later by Hains (1967), Reynolds & Potter (1967) and Cowley & Smith (1985). The results are typically understood with respect to a Reynolds number that is based on the maximal velocity of the Poiseuille component, say R_p, and the ratio of wall velocity to maximal velocity of the Poiseuille component denoted by k. For small Couette components, k, it is possible to observe some destabilization of the flow (depending on the wavenumber), but as soon as $k > 0.3$ a strong stabilization of the flow sets in. As the velocity ratio k exceeds 0.7, the neutral stability curve completely vanishes and the flow becomes unconditionally linearly stable, i.e. $R_c \rightarrow \infty$. The term ‘cutoff’ velocity has been used to describe this stabilization; see Reynolds & Potter (1967).

Although plane Couette flows are widely studied, it is worth noting that they are actually difficult to produce, i.e. outside of the computational and theoretical domain. In many duct flows, axial translation of a wall is either not possible or limited in terms of speed. High R frequently means high velocities, lowering the range of achievable k as the flow velocity increases. Therefore, the range of practical flows for which a sufficiently stabilizing Couette component can be introduced is limited and we know of no technological applications where this is used for stabilization.

Annular Couette–Poiseuille (ACP) flows are more practically relevant and have also been studied extensively (Mott & Joseph 1968; Sadeghi & Higgins 1991). For example, ACP flows occur when removing/inserting drillpipe or casing from vertical wellbores during an operation called ‘tripping’. Sadeghi & Higgins (1991) studied the flow between two concentric cylinders, the outer being stationary while the inner is moved with a constant (dimensionless) velocity k in the streamwise direction. They showed that varying the radius ratio (η) between the outer and inner cylinders can have a dramatic effect on the stability characteristics. The limit $\eta \rightarrow 1$ approximates PCP flow and is unconditionally linearly stable for $k \geqslant 0.7$, thereby confirming Potter (1966). By increasing η, the cutoff condition is attained for lower values of k and the cutoff relation between k–η is almost linear. Similar to Mott & Joseph (1968), they argued that increasing η increases the asymmetry of the base flow profile which in turn increases the stability with respect to axisymmetric disturbances. Their findings are very relevant to our work, because we later show that the stability achieved by increasing η in ACP flows and that achieved by applying a small crossflow in PCP flows are essentially similar.

Shear flows with crossflow occur in a range of natural settings as well as in various technological applications. As examples, we cite studies in sediment–water interfaces over permeable seabeds (Goharzadeh, Khalili & Jrgensen 2005), fluid transport and consequent mass transfer at the walls of blood vessels, the lungs and kidneys (Majdalani, Zhou & Dawson 2002), and flow through the fractures of geological formations (Berkowitz 2002). In some technological applications, crossflow is an inherent part of the process, e.g. dewatering of pulp suspensions in paper making, whereas in others it is introduced to affect the stability. An example of the latter is the use of wall suction to delay the transition to turbulence over the surface of an aircraft wing (Joslin 1998).

The stability of PP flow with crossflow was first analysed by Hains (1971) and Sheppard (1972), both of whom have shown that a modest amount of crossflow produces a significant increase of the critical Reynolds number. These results are however slightly problematic to interpret in absolute terms, because at a fixed pressure gradient along the channel, increasing the crossflow decreases the velocity along the channel (hence effectively the Reynolds number). This difficulty was noted by Fransson & Alfredsson (2003), who used the maximal channel velocity as their velocity scale (instead of that based on the PP flow without crossflow), and thus separated the effects of base velocity magnitude from those of the base velocity distribution. Using this velocity scale in their Reynolds number R, they showed regimes of both stabilization and destabilization as the crossflow Reynolds number was increased. For example, for $R = 6000$ and wavenumber $\alpha = 1$, Fransson & Alfredsson (2003) have shown that the crossflow was stabilizing up to a crossflow Reynolds number $R_{inj} \approx 3.4$, and then starts destabilizing before re-stabilizing again at $R_{inj} \approx 635$. The initial regime of stabilization is the one corresponding to the earlier results.

Although crossflow affects the base velocity profile, the main change to the linear stability problem is to add an inertial crossflow term to the Orr–Sommerfeld operator. One reason why addition of terms such as the crossflow term can destabilize an otherwise stable shear flow is suggested by the two-dimensional instability of the Blasius boundary layer, as studied by Baines, Majumdar & Mitsudera (1996). In such flows, the resulting growing disturbance is known as a Tollmien–Schlichting (T-S) wave. They showed that the interaction between two idealized modes, viz. an ‘inviscid’ neutral mode at zero viscosity and a decaying viscous mode (or modes) existing at uniform shear, undergoes resonant interactions. The latter is forced by the former through the no-slip wall boundary conditions.

In this study, we focus on the combination of crossflow and Couette component. Our motivation stems from a desire to understand how the two mechanisms interact, because in terms of technological application different mechanical configurations may be more or less amenable to crossflow and/or wall motion. This means that it is useful to know when one effect may compensate for the other in stabilizing (or destabilizing) a given flow. To our knowledge, the stability of PCP flow with crossflow has only been studied in any generality by Hains (1971). In considering the base flow for PCP flow with crossflow (which is parameterized by R_{inj} and k), the relation $kR_{inj} = 4$ defines an interesting paradigm in which the base velocity in the axial direction is linear. These Couette-like flows have been studied by Nicoud & Angilella (1997) for increasing R_{inj}. They found a critical value of $R_{inj} \approx 24$, below which no instability occurs (we have translated their critical value of 48 into the R_{inj} that we use). Therefore, we observe that an understanding of crossflow PCP flows is far from complete. We aim at contributing to this understanding.

The three-dimensional linear stability of PCP flow with crossflow is amenable to Squires transformation, so that the linear instability occurs first for two-dimensional (spanwise-independent) perturbations. We study these perturbations here. Our aim is to demarcate clearly in the (R_{inj}, k)-plane, regions of unconditional stability, i.e. where there is a cutoff wall velocity or injection velocity. We also wish to understand the underlying linear stability mechanisms as R_{inj} and k are varied.

Although the study of two-dimensional perturbations is justified from the pure perspective of linear stability, three-dimensional and nonlinear effects are likely to be relevant in instabilities that are observed to grow, i.e. the actual transition. The past two decades have seen an extensive study of transient growth mechanisms, because of non-normality of the operator associated with linearized Navier–Stokes equations. Algebraic growth of $O(R^2)$ may occur for linearly stable disturbances that decay only slowly over a time scale of $O(R)$. It has been proposed that this transient algebraic growth is responsible for subcritical transition in wall-bounded shear flows. For an overview of these developments, we refer to Reddy, Schmid & Henningson (1993), Schmid & Henningson (2001), Chapman (2002) and Schmid (2007).

At the same time as transient growth mechanisms have undergone extensive research, self-sustaining nonlinear mechanisms were proposed by Waleffe and others (Hamilton, Kim & Waleffe 1995; Waleffe 1997). In this scenario, energy from the mean flow can be fed back into streamwise vortices, thus resisting viscous decay. Self-sustained exact unstable solutions to the Navier–Stokes equations were found by Faisst & Eckhardt (2003) and Wedin & Kerswell (2004). Much current effort is focused on understanding the link between these self-sustained unstable solutions and observed transitional phenomena, such as intermittency, streaks, puffs and slugs (see e.g. Hof *et al.* 2004, 2005; Eckhardt *et al.* 2007; Kerswell & Tutty 2007).

Our study does not deal with any of the complexities of transition mentioned above, and as such the relevance may be questioned. This is a fair criticism, but, on the other hand, we note that for other classical shear flows that are linearly stable at all R, careful control of apparatus imperfections and the level of flow perturbations can significantly retard the point at which transition is observed. For example, in Hagen–Poiseuille flow of Newtonian fluids, one typically observes transition to turbulence starting for $R \gtrsim 2000$. However, an experimental flow loop in Manchester, UK, produces stable laminar flows for $R \approx 24\,000$ (Hof *et al.* 2004; Peixinho & Mullin 2006), and stable flows have even been reported up to $R \approx 100\,000$ (Pfenniger 1961). This all suggests that a significantly enhanced stability may be achieved experimentally, where predicted by the linear theory.

The question of how to achieve a PCP flow with crossflow in practice is also relevant. Evidently all Poiseuille flows occur in finite geometries with entrance effects, sidewalls and imperfections in the planar walls, so that the notion of a truly planar infinite flow is anyway flawed. Uniform base flows studied in hydrodynamic stability are invariably an approximation of experimental reality. Even in the absence of wall motion, a planar Poiseuille flow is difficult experimentally, due to spanwise perturbations and inflow non-uniformities. This said, a geometry with a uniformly translating channel wall is particularly difficult to achieve and as mentioned before, $k \approx 0.7$ is difficult for high R flows where R is increased via flow rate. Imposing a uniform crossflow along with a streamwise pressure variation is more practically achievable (see e.g. Vadi & Rizvi 2001). A uniform trans-membrane pressure crossflow micro-filtration system is able to maintain uniform trans-membrane pressure with high crossflow velocity ($\hat{V}_{inj}$) and improves the utilization of available filtration area. In the patent of Sandblom (2001) the concept of operating a membrane filtration unit using UTMP has been proposed, such that pressure drop along the channel can be adjusted independent of $\hat{V}_{inj}$. A different generic concept for achieving a uniform crossflow over a finite length of a porous-walled channel consists of injecting the fluid along a secondary channel behind one of the porous walls that has a linearly converging geometry. Although there are clear technical challenges, it is worth remarking that the injection velocities needed for stability are very modest by comparison with the wall velocities, and therefore as a target appear achievable.

An outline of the paper is as follows. In § 2, we introduce the base flow and linear stability problem. We describe the numerical method and present benchmark results that illustrate typical effects of varying R_{inj} and k. These results serve to motivate the presentation of results, which follows in three sections. Section 3 considers low R_{inj} and significant k, where we see that long wavelengths dominate. In § 4, we characterize the flows for intermediate R_{inj} and small k, where short wavelengths are the least stable. Finally, we consider large R_{inj} in § 5, where both destabilization and eventual stabilization are found. In § 6, we conclude with a summary of the principal results.

2. Stability of plane Couette–Poiseuille flow with crossflow

The base flow considered in this paper is a PCP flow with imposed uniform crossflow. This flow is two-dimensional, viscous, incompressible and fully developed in the streamwise direction, $\hat{x}$ (all dimensional variables are denoted by a 'hat'). The imposed base velocity $\hat{v}$ in the $\hat{y}$-direction is constant and equal to the injection/suction velocity $\hat{V}_{inj}$. Because $\hat{v}$ is constant, the $\hat{x}$-component of velocity, $\hat{u}$ depends only on $\hat{y}$. The flow domain is bounded by walls at $\hat{y} = \pm\hat{h}$ and is driven in the $\hat{x}$-direction by a constant pressure gradient and translation of the upper wall, at speed $\hat{U}_c$. The $\hat{x}$-component of velocity, $\hat{u}(\hat{y})$, is found from the $\hat{x}$-momentum equation, which simplifies to

$$\hat{V}_{inj}\frac{\partial \hat{u}}{\partial \hat{y}} = -\frac{1}{\hat{\rho}}\frac{\partial \hat{p}}{\partial \hat{x}} + \hat{\nu}\frac{\partial^2 \hat{u}}{\partial \hat{y}^2}, \tag{2.1}$$

where $\hat{\rho}$ is the density, $\hat{\nu} = \hat{\mu}/\hat{\rho}$ is the kinematic viscosity, and $\hat{\mu}$ is the dynamic viscosity. The boundary conditions at $\hat{y} = \pm\hat{h}$ are

$$\hat{u}(-\hat{h}) = 0, \quad \hat{u}(\hat{h}) = \hat{U}_c. \tag{2.2}$$

To scale the problem we scale all lengths with $\hat{h}$; hence $(x, y) = (\hat{x}/\hat{h}, \hat{y}/\hat{h})$. For the velocity scale two choices are common. First, the imposed pressure gradient defines a 'Poiseuille' velocity scale:

$$\hat{U}_p = -\frac{\hat{h}^2}{2\hat{\mu}}\frac{\partial \hat{p}}{\partial \hat{x}}, \tag{2.3}$$

which is equivalent to the maximum velocity of the plane Poiseuille flow, driven by the pressure gradient alone. Second, we may take the maximum velocity, which we need to compute. $\hat{U}_p$ is the choice of Potter (1966), and thus allows one to compare directly with the studies of PCP flows. In the absence of a crossflow, the maximal velocity is not actually very sensitive to the wall velocity $\hat{U}_c$, at least for $\hat{U}_c < \hat{U}_p$, which covers the range over which the flow stabilizes. However, in the case of a strong crossflow, the $\hat{x}$-velocity is reduced significantly below $\hat{U}_p$, which therefore loses its meaning. Consequently, we adopt the second choice and scale with the maximal velocity, $\hat{U}_{max}$. This choice retains physical meaning in the base velocity, but does introduce algebraic complexity.

The solution is found from (2.1) and (2.2) after detailed but straightforward algebra:

$$\hat{u}(\hat{y}) = \hat{U}_p \left[\frac{4\cosh R_{inj} - kR_{inj}\mathrm{e}^{-R_{inj}} + [kR_{inj} - 4]\mathrm{e}^{R_{inj}\hat{y}/\hat{h}}}{2R_{inj}\sinh R_{inj}} + \frac{2\hat{y}}{R_{inj}\hat{h}} \right], \tag{2.4}$$

where k and R_{inj} are defined by

$$k = \frac{\hat{U}_c}{\hat{U}_p}, \tag{2.5}$$

$$R_{inj} = \frac{\hat{V}_{inj}\hat{h}}{\hat{\nu}}. \tag{2.6}$$

These two dimensionless parameters uniquely define the dimensionless base flow. The parameter k is the velocity ratio of Couette to Poiseuille velocities, which is useful as it allows direct comparison with earlier results on the stabilization of PCP flows without crossflow. The parameter R_{inj} is simply a Reynolds number based on the injection velocity. Primarily, here we consider the ranges $k \in [0, 1]$ and $R_{inj} \geqslant 0$.

For relatively weak crossflow velocities, the velocity component $u(y)$ has a single maximum at a value of $y = y_{max}$ defined by

$$\mathrm{e}^{R_{inj}y_{max}} = \frac{\sinh R_{inj}}{R_{inj}} \frac{4}{4 - kR_{inj}}. \tag{2.7}$$

The maximal velocity $\hat{U}_{max}$ is then evaluated from (2.4). Because $\sinh R_{inj} \geqslant R_{inj}$, we can see that $y_{max} > 0$ for $k \geqslant 0$ and $R_{inj} > 0$. Both the injection crossflow and Couette component act to skew the velocity profile towards the upper wall. For stronger crossflow velocities (or sufficiently large k), the maximal velocity occurs at the upper wall, i.e. $\hat{U}_{max} = \hat{U}_c$.

The division between weak and strong crossflows, taking into account also the Couette component, is defined by

$$kR_{inj} = 4\left[1 - \frac{\sinh R_{inj}}{R_{inj}\mathrm{e}^{R_{inj}}}\right]. \tag{2.8}$$

The dimensionless base velocity is given by

$$u(y) = \begin{cases} \dfrac{4\cosh R_{inj} - kR_{inj}\mathrm{e}^{-R_{inj}} - [4 - kR_{inj}]\mathrm{e}^{R_{inj}y} + 4y\sinh R_{inj}}{4\cosh R_{inj} - kR_{inj}\mathrm{e}^{-R_{inj}} - [4 - kR_{inj}]\mathrm{e}^{R_{inj}y_{max}} + 4y_{max}\sinh R_{inj}}, \\ \qquad\qquad kR_{inj} \leqslant 4\left[1 - \dfrac{\sinh R_{inj}}{R_{inj}\mathrm{e}^{R_{inj}}}\right], \\ \dfrac{1}{k}\left[\dfrac{4\cosh R_{inj} - kR_{inj}\mathrm{e}^{-R_{inj}} - [4 - kR_{inj}]\mathrm{e}^{R_{inj}y}}{2R_{inj}\sinh R_{inj}} + \dfrac{2y}{R_{inj}}\right], \\ \qquad\qquad kR_{inj} > 4\left[1 - \dfrac{\sinh R_{inj}}{R_{inj}\mathrm{e}^{R_{inj}}}\right]. \end{cases} \tag{2.9}$$

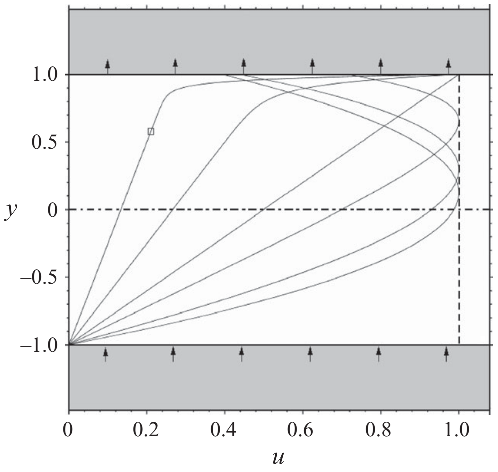

FIGURE 1. Mean velocity distribution for $k = 0.5$ and $R_{inj} = 0$, 1, 4, 8, 15 and 30 ($R_{inj} = 30$ denoted by □).

It can be verified that in the limit $R_{inj} \rightarrow 0$, with k fixed, the classical form of PCP base velocity profile is retrieved:

$$u(y) \sim \frac{1 - y^2 + \dfrac{k}{2}(1 + y) + R_{inj}\left[\dfrac{1}{3}(y - y^3) - \dfrac{k}{4}(1 - y^2)\right]}{1 + \dfrac{k}{2} + \dfrac{k^2}{16} - R_{inj}\left[\dfrac{k}{6} - \dfrac{k^3}{64}\right]} \tag{2.10}$$

as $R_{inj} \rightarrow 0$, with $k \leqslant 4[1 - \sinh R_{inj}/(R_{inj}\mathrm{e}^{R_{inj}})]/R_{inj} \sim 4[1 + R_{inj}/3]$.

Examples of the base velocity profile are given in figure 1, for $k = 0.5$ and different values of R_{inj}. Note that for $R_{inj} = 8$, when $kR_{inj} = 4$, the velocity profile is linear. This flow has been termed a 'generalized Couette' flow by Nicoud & Angilella (1997).

We shall denote differentiation with respect to y by the operator D. The first and second derivatives of the base flow, $\mathrm{D}u$ and D^2u respectively, influence the stability of the flow. We find that D^2u has sign determined by $(kR_{inj} - 4)$ and increases in absolute value exponentially towards the upper wall. For $kR_{inj} < 4$, the velocity is concave and is convex otherwise. Because D^2u does not change sign, the maximal absolute value of the first derivative is found at either the upper or lower wall, $y = \pm 1$. The maximal velocity gradients are found at the lower wall for small R_{inj} and also for a range of R_{inj} close to $kR_{inj} = 4$, but otherwise are found at $y = 1$; see figure 2(*a*). At large R_{inj}, the maximal velocity increases almost linearly:

$$|\mathrm{D}u|_{max} = |\mathrm{D}u(y = 1)| = \frac{1}{k}\left[\frac{[kR_{inj} - 4]\mathrm{e}^{R_{inj}}}{2\sinh R_{inj}} + \frac{2}{R_{inj}}\right] \sim R_{inj} - \frac{4}{k} + \frac{2}{kR_{inj}} + O(\mathrm{e}^{-2R_{inj}}). \tag{2.11}$$

Figure 2(*b*) shows examples of the profiles of D^2u. We observe that $\mathrm{D}^2u \approx 0$ over a large range of y, close to the lower wall, whenever a significant amount of crossflow is present, i.e. $R_{inj} \gtrsim 1$.

2.1. *Dimensionless groups*

The base flow is fully defined by the parameters k and R_{inj}, as discussed above. In addition, the transient flow and associated stability problem will depend on the

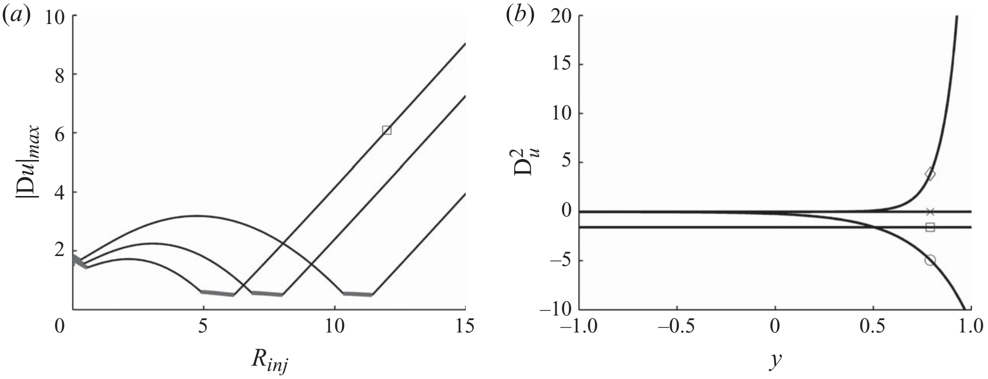

FIGURE 2. (a) Maximal velocity gradient, $|\mathrm{D}u|_{max}$, plotted against R_{inj} for $k=0.35$, 0.5, 0.65 ($k=0.65$ denoted by □). The thick line indicates where the maximum is attained at $y=-1$; otherwise at $y=1$. (b) Variation of D^2u with y for $k=0.5$ for $R_{inj}=0$ (□); $R_{inj}=4$ (○); $R_{inj}=8$ (×); $R_{inj}=12$ (◇).

streamwise Reynolds number, R, which we define in terms of $\hat{U}_{max}$, i.e.

$$R=\frac{\hat{U}_{max}\hat{h}}{\hat{\nu}}. \tag{2.12}$$

To aid the reader in interpreting our results in terms of those previously published, it is helpful to consider also a Reynolds number based on the Poiseuille velocity, $\hat{U}_p$, say $R_p=\hat{U}_p\hat{h}/\hat{\nu}$. Straightforwardly, we find $R=R_pF(k,R_{inj})$:

$$F(k,R_{inj})=\begin{cases}\dfrac{4\cosh R_{inj}-kR_{inj}\mathrm{e}^{-R_{inj}}+[kR_{inj}-4]\mathrm{e}^{R_{inj}y_{max}}+4y_{max}\sinh R_{inj}}{2R_{inj}\sinh R_{inj}}, & \\ \qquad kR_{inj}\leqslant 4\left[1-\dfrac{\sinh R_{inj}}{R_{inj}\mathrm{e}^{R_{inj}}}\right], & \\ k, \quad kR_{inj}>4\left[1-\dfrac{\sinh R_{inj}}{R_{inj}\mathrm{e}^{R_{inj}}}\right]. & \end{cases} \tag{2.13}$$

Note that $F(k,R_{inj})=\hat{U}_{max}/\hat{U}_p$, which is fixed by the parameters k and R_{inj}. Thus, for fixed k and R_{inj} an increase in R is interpreted as an increase in R_p and vice versa. It is also useful to know the ratio of upper wall velocity to the maximal velocity, i.e. $\hat{U}_c/\hat{U}_{max}$, which we shall denote by $\tilde{k}$, given simply by the ratio $k/F(k,R_{inj})$:

$$\tilde{k}(k,R_{inj})=\begin{cases}\dfrac{2kR_{inj}\sinh R_{inj}}{4\cosh R_{inj}-kR_{inj}\mathrm{e}^{-R_{inj}}+[kR_{inj}-4]\mathrm{e}^{R_{inj}y_{max}}+4y_{max}\sinh R_{inj}}, & \\ \qquad kR_{inj}\leqslant 4\left[1-\dfrac{\sinh R_{inj}}{R_{inj}\mathrm{e}^{R_{inj}}}\right], & \\ 1, \quad kR_{inj}>4\left[1-\dfrac{\sinh R_{inj}}{R_{inj}\mathrm{e}^{R_{inj}}}\right]. & \end{cases} \tag{2.14}$$

The ratio R/R_p and the upper wall speed $\tilde{k}$ are illustrated in figure 3 for convenience.

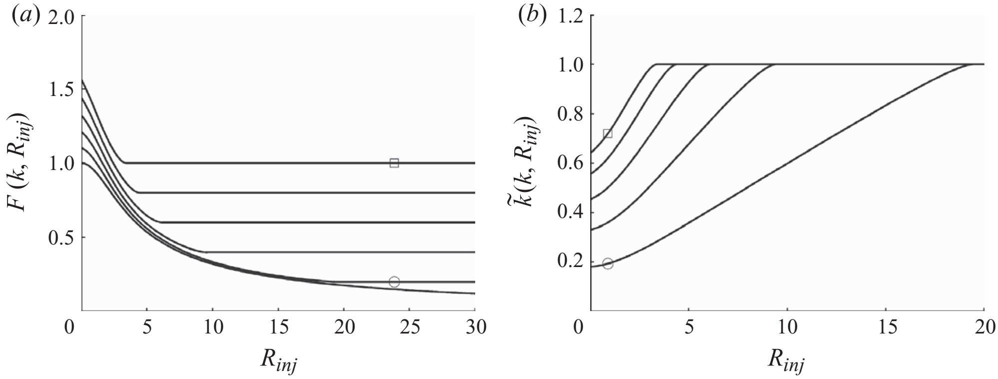

FIGURE 3. (*a*) $R/R_p = F(k, R_{inj})$ for $k = 0$, 0.2, 0.4, 0.6, 0.8, 1; (*b*) dimensionless wall speed $\tilde{k}(k, R_{inj})$ for $k = 0.2$, 0.4, 0.6, 0.8, 1. Symbols: ○, $k = 0.2$; □, $k = 1$.

2.2. *The stability problem*

The base flow is two-dimensional, but because $v = R_{inj}$ is constant, the three-dimensional linear stability equations are only modified by the addition of a constant convective term:

$$R_{inj}\frac{\partial}{\partial y}\boldsymbol{u}',$$

where $\boldsymbol{u}' = (u', v', w')$ denotes the linear perturbation. The classical Squire transformation can therefore be applied to the temporal problem, showing that for any unstable three-dimensional linear disturbance there exists an unstable two-dimensional linear disturbance at lower R; see Squire (1933).

It suffices to consider only two-dimensional disturbances and we adopt the usual normal mode approach to linear spatially periodic perturbations, introducing a streamfunction that we represent in modal form as

$$\hat{\psi}(x, y, t) = \phi(y)\mathrm{e}^{[\mathrm{i}\alpha(x-ct)]}, \qquad (2.15)$$

with $u' = \mathrm{D}\phi(y)\mathrm{e}^{[\mathrm{i}\alpha(x-ct)]}$, $v' = -\mathrm{i}\alpha\phi(y)\mathrm{e}^{[\mathrm{i}\alpha(x-ct)]}$. Thus, α is real, denoting the wavenumber, c denotes the complex wave speed, ($c = c_r + \mathrm{i}c_i$, $\mathrm{i} = \sqrt{-1}$), and $\phi(y)$ denotes the amplitude of the streamfunction perturbation. The modified Orr–Sommerfeld (O-S) equation for the flow is

$$\mathrm{i}\alpha R[(c-u)(\alpha^2 - \mathrm{D}^2) - \mathrm{D}^2u]\phi - R_{inj}\mathrm{D}(\alpha^2 - \mathrm{D}^2)\phi = (\alpha^2 - \mathrm{D}^2)^2\phi, \qquad (2.16)$$

and the boundary conditions are

$$\phi(\pm 1) = \mathrm{D}\phi(\pm 1) = 0. \qquad (2.17)$$

The inclusion of the injection crossflow results in additional third-order derivatives in the inertial terms, i.e. $R_{inj}\mathrm{D}(\alpha^2 - \mathrm{D}^2)\phi$. Note that R_{inj} also influences stability via the base velocity profile $u(y)$. Equations (2.16) and (2.17) constitute the eigenvalue problem. The eigenvalue c is parameterized by the four dimensionless groups (α, R, R_{inj}, k) and the condition of marginal stability is

$$c_i(\alpha, R, R_{inj}, k) = 0. \qquad (2.18)$$

We attempt to characterize the stability of (2.16) and (2.17) for positive (α, R, R_{inj}, k). We may note that the limit $R \to \infty$ for finite R_{inj} reduces (2.16) to the Rayleigh equation. Because D^2u is of one sign only, there are no inflection points and hence no purely inviscid instability. This suggests that the instabilities of (2.16) and (2.17) will be viscous in nature.

The addition of the constant crossflow terms does not fundamentally alter the O-S problem, and we expect a discrete spectrum. To find the spectrum of (2.16) and (2.17), we use a spectral approach, representing ϕ by a truncated sum of Chebyshev polynomials:

$$\phi = \sum_{n=0}^{N} a_n T_n(y) \quad \text{for} \quad y \in [-1, 1], \tag{2.19}$$

where N is the order of the truncated polynomial, a_n is the coefficient of the nth Chebyshev polynomial $T_n(y)$. This method is described for example by Schmid & Henningson (2001) and is widely used. The discretized problem is coded and solved in Matlab. The accuracy of the code has been checked against the results of Mack (1976) for the Blasius boundary layer, with various results for PP flow in Schmid & Henningson (2001), with the PCP flow results of Potter (1966), and finally against results for PP flow with crossflow (see Sheppard 1972; Fransson & Alfredsson 2003). The results are accurate up to three, four and five significant places when validated against Potter (1966), Mack (1976) and Fransson & Alfredsson (2003), respectively. All the numerical results given below have been computed with $N = 120$. On using 200 collocation points, the growth rates changed only in the fourth significant place in the worst case.

2.3. *Characteristic effects of varying k and R_{inj}*

Before starting a systematic analysis of (2.16) and (2.17), we briefly show some example results that illustrate the characteristic effects of varying the Couette component, k, and the crossflow component, R_{inj}. These examples also serve to establish the framework of analysis used later in the paper. With reference to PP flow, Potter (1966) first observed that the stability is increased by adding a Couette component while Fransson & Alfredsson (2003) showed that crossflow can stabilize or destabilize PP flow.

2.3.1. *Eigenspectra*

Setting $(\alpha, R) = (1, 6000)$, we investigate variations in the eigenspectrum of (2.16) and (2.17). According to a classification proposed by Mack (1976), the spectrum of PP flow may be divided into three distinct families: A, P and S. Family A exhibits low phase velocity and corresponds to the modes concentrated near the fixed walls. Family P represents phase velocities c_r close to the maximum velocity in the channel. Family S corresponds to the mean modes and has phase velocity c_r close to the mean velocity. In figures 4(*a*) and 4(*b*), we track the eigenmodes as k and R_{inj}, respectively, are varied from zero. The initial condition (denoted by a square) represents the PP flow.

Referring to figure 4(*a*) (where $R_{inj} = 0$), addition of the Couette component increases the mean velocity: the S modes shift from $c_r = 0.6667$ at $k = 0$ (PP flow) to $c_r = 0.7513$ at $k = 1$. The family of P modes is also shifted to the right. The A modes are associated with both walls, and as k increases we see a splitting of the family, with the upper wall modes moving to the right as k is increased. The least stable mode is a wall mode associated with the lower wall, which we observe stabilizes monotonically as k is increased. Figure 4(*b*) shows the effects of increasing R_{inj} (holding $k = 0$). The least stable A mode of PP flow initially stabilizes and then destabilizes with

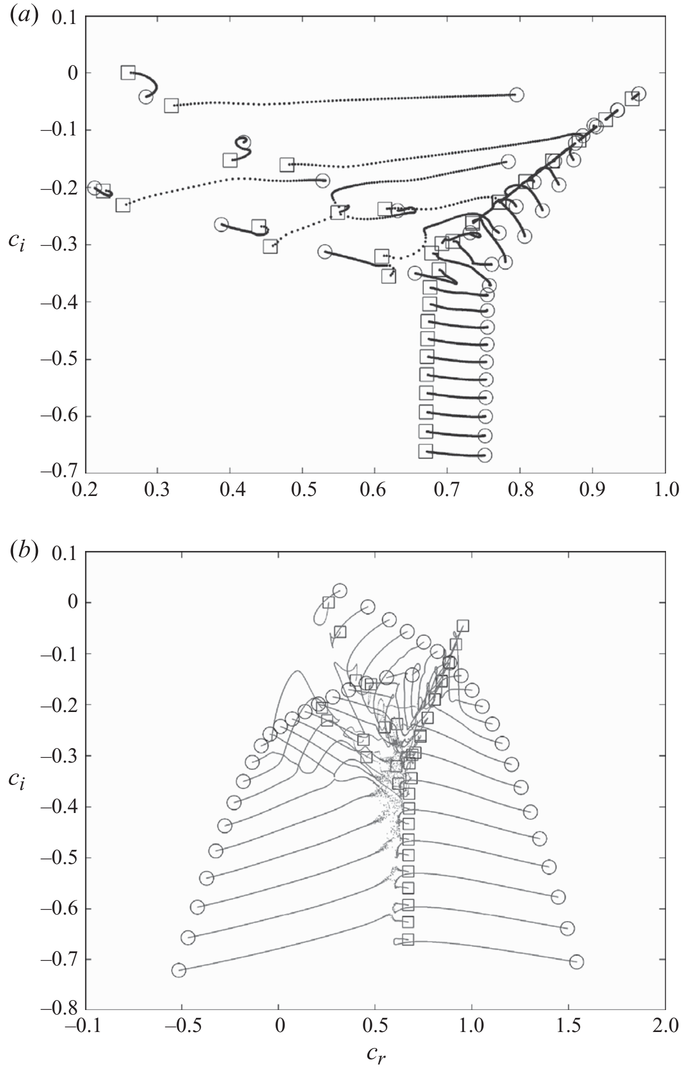

FIGURE 4. Eigenspectrum of $(\alpha, R) = (1, 6000)$ by varying k and R_{inj}. Forty least stable modes are considered. (a) Effect of increasing k from 0 to 1 in steps of 0.01, keeping $R_{inj} = 0$. (b) Effect of increasing R_{inj} from 0 to 100 in steps of 0.05, keeping $k = 0$ (PP flow). Symbols: □, $k = 0$ or $R_{inj} = 0$; ○, $k = 1$ or $R_{inj} = 100$; . . . , intermediate k or R_{inj}. The PP flow spectrum, represented by □ in both figures, shows the vertical family of S-modes, the branch of A-modes (diagonally upwards from centre to left) and branch of P-modes (diagonally upwards from centre to right).

increasing R_{inj}. This particular behaviour has also been observed by Fransson & Alfredsson (2003). For large R_{inj}, the A, P and S families have disappeared, instead leaving two distinct families of modes. It appears that each of the A, P and S families splits, with some modes entering each of the two families (this alternate splitting is most evident for the S modes). As observed by Nicoud & Angilella (1997), the phase speed no longer lies in the range of the axial velocity. This does not violate the conditions on c_r, given by Joseph (1968) and Joseph (1969), because these conditions are derived for parallel flows only.

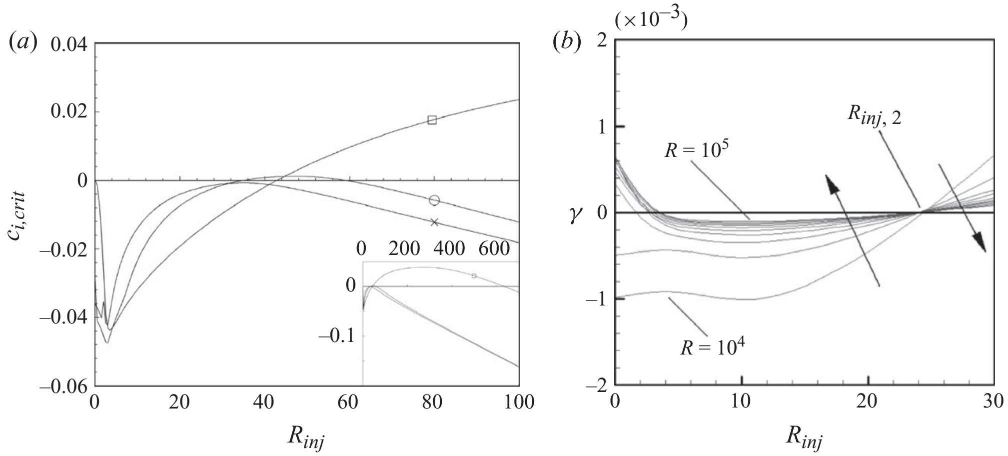

FIGURE 5. (*a*) Effect of increasing R_{inj} on the stability of PCP flow, for $(\alpha, R) = (1, 6000)$ and different values of $k = 0\,(\square)$, $0.5\,(\bigcirc)$, $1\,(\times)$. (*b*) Maximal growth rate for increasing R_{inj} at different R, ($k = 0.5$ and the step in values of R between curves is 10^4).

2.3.2. *Increasing R_{inj}*

Next, we illustrate the qualitative effects of increasing R_{inj} at fixed (α, R, k) in figure 5(*a*). We again fix $\alpha = 1$ and $R = 6000$, and show the variation of the least stable eigenvalue, for $k = 0$, 0.5, 1. Our results for $k = 0$ (PP flow) may be compared directly with those of Fransson & Alfredsson (2003). We observe that as R_{inj} increases we have an initial range of stabilization ($c_{i,crit}$ decreasing), followed by a range of destabilization ($c_{i,crit}$ increasing), and finally again stabilization at large R_{inj} ($c_{i,crit}$ decreasing). Qualitatively, we have observed these same three ranges of decreasing/increasing $c_{i,crit}$, as R_{inj} increases, for all numerical results that we have computed, and this provides a convenient framework within which to describe our results.

For fixed (α, R, k), the case $R_{inj} = 0$ may be either stable or unstable, in which cases there are respectively two or three marginal stability values of R_{inj}. We denote these marginal values of R_{inj} by $R_{inj,1}$, $R_{inj,2}$, $R_{inj,3}$, noting that when $R_{inj} = 0$ is stable $R_{inj,1}$ is absent. More clearly, $R_{inj,2}$ will always represent a transition from stable to unstable, while $R_{inj,1}$ and $R_{inj,3}$ denote transitions from unstable to stable. The PCP flows for $k = 0.5$ and 1 are stable for $(\alpha, R) = (1, 6000)$ in the absence of crossflow, $R_{inj} = 0$. For a larger R, $k = 0.5$ is unstable at $R_{inj} = 0$, but $k = 1$ remains stable for all (α, R).

Figure 5(*b*) shows the maximal growth rate γ, for increasing R_{inj} at different R, with $k = 0.5$. The maximal growth rate is computed over wavenumbers $\alpha \in [0, 1]$:

$$\gamma = \max_{\alpha \in [0,1]} \{\alpha c_i\}, \tag{2.20}$$

which often captures the largest growth rates over all α. We observe that the first marginal value $R_{inj,1}$ increases with R, but appears to converge towards a finite value as $R \to \infty$. The second marginal value of $R_{inj,2}$ appears independent of R (at least numerically). For $k = 0.5$ we have $R_{inj,2} \approx 24.7$. Nicoud & Angilella (1997) have observed a similar behaviour in studying the generalized Couette flow (for which the constraint, $kR_{inj} = 4$, is always satisfied). They have found $R_{inj,2} \approx 24$ (note that Nicoud & Angilella (1997) use the full channel width as their length scale, and therefore report $R_{inj,2} \approx 48$, in their variables). In contrast, the third marginal value,

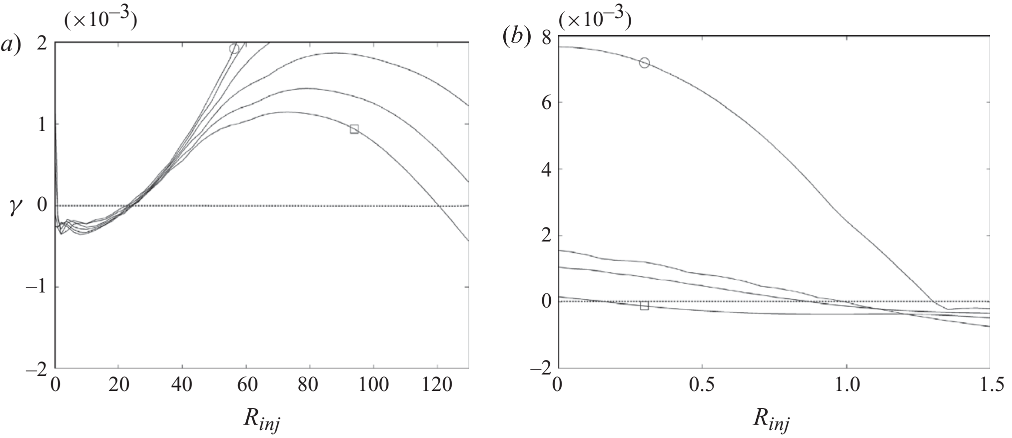

FIGURE 6. Maximal growth rate versus R_{inj} at $R = 40\,000$: (a) $R_{inj,2}$ and $R_{inj,3}$ for $k = 0$ (○) to 1 (□); (b) $R_{inj,1}$ for $k = 0$ (○) to 0.6 (□). Step size is 0.2 in both figures.

$R_{inj,3}$, is strongly dependent on R. For example, for $k = 0.5$, the values corresponding to $R = 10\,000$ and $100\,000$ are $R_{inj,3} \approx 83$ and $R_{inj,3} \approx 287$, respectively.

2.3.3. *Increasing k*

Figure 6 explores the effects of increasing the Couette component k, on γ and on the marginal values of R_{inj}. Figure 6(a) indicates that the sensitivity of $R_{inj,2}$ to k is also not extreme: we have found that this transition occurs within the range ∼22–25 for $k \in [0, 1]$. For each value of k examined, we also observe numerically a similar independence of $R_{inj,2}$ from R as seen earlier in figure 5(b) for $k = 0.5$. The third marginal value, $R_{inj,3}$, is strongly dependent on k. For example, at $R = 40\,000$, $R_{inj,3}(k = 1) \approx 120$ and $R_{inj,3}(k = 0.8) \approx 135$. In general, increasing k shifts $R_{inj,3}$ to the left, thereby decreasing the span of the unstable region. Increasing k also decreases the maximum value of γ.

Figure 6(b) looks at the first transition, $R_{inj,1}$ at $R = 40\,000$. Potter (1966) was the first to observe that for PCP flows (i.e. $R_{inj} = 0$), a gradual increase in the wall velocity results in crossing a 'cutoff' value of k, say k_1, such that for $k > k_1$ the flow is unconditionally linearly stable. It has already been pointed out from the results of figure 5(b) that $R_{inj,1}$ is finite as $R \to \infty$. In addition, the results in figure 6(b) indicate that $R_{inj,1}$ decreases with k at a finite R. Hence, it can be inferred that as $R \to \infty$, the cutoff wall velocity, $k_1 = k_1(R_{inj})$, must decrease with R_{inj}.

3. PCP flows and the effects of small R_{inj}

Having developed a broad picture of the different transitions occurring in the flow, we now focus in depth on each range of R_{inj}, to understand the stability mechanisms in play. We start with the range of small R_{inj}.

PCP flows without crossflow are stable to inviscid modes, but viscosity admits additional modes, i.e. the T-S waves, which may destabilize, according to the value of k. When $\alpha R \gg 1$ with $c \sim O(1)$, viscous effects occur in thin oscillatory layers: (i) adjacent to the walls (of thickness $\sim(\alpha R)^{-1/2}$) and (ii) close to the critical point(s), y_c, where $u(y_c) = c_{r,crit}$ are found (of thickness $\sim(\alpha R)^{-1/3}$). It is in the critical layers that we see peaks in the distribution of energy production, implying transfer from the base flow. Potter (1966) put forward the argument that for a dimensionless wall

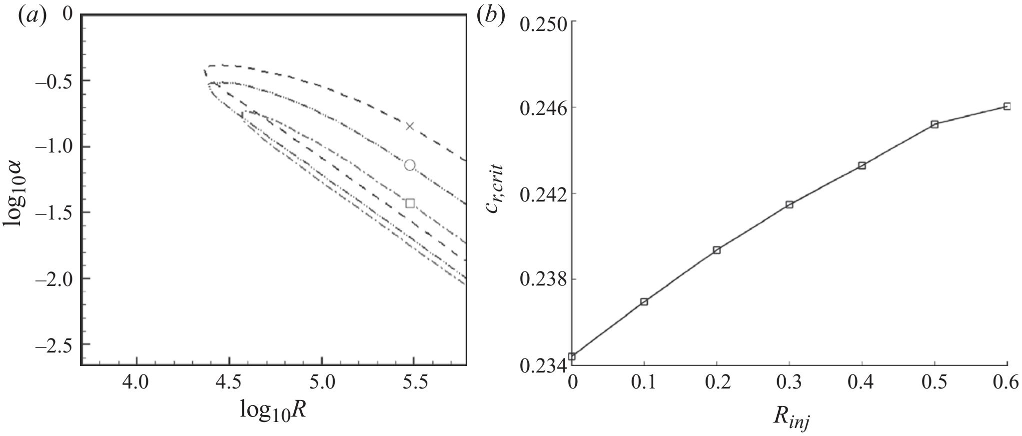

FIGURE 7. Critical values for $k=0.5$: (a) neutral stability curves for $R_{inj}=0\,(\times)$, $0.3\,(\bigcirc)$ and $0.53\,(\square)$; (b) variation in $c_{r,crit}$ with R_{inj}.

velocity that exceeds $c_{r,crit}$, the critical layer near the moving wall will vanish and there remains only one critical layer, near the fixed lower wall. The thickness of this second layer increases with wall velocity, thereby favouring stabilization.

This mechanism appears to correctly describe the long-wavelength perturbations (at $R_{inj}=0$), which are found to be the least stable for $k \sim O(1)$. Indeed Cowley & Smith (1985) developed a long-wavelength analysis ($\alpha \sim R$) in order to predict the cutoff value $k_1(R_{inj}=0) \approx 0.7$. For values $k \sim O(1)$, PCP flows have only a single neutral stability curve (NSC). However, Cowley & Smith (1985) noted that for smaller k, multiple neutral stability curves could exist, and at shorter wavelengths. For example, when $0 \leqslant k \leqslant R^{-2/7}$ there is one NSC, when $R^{-2/7} \leqslant k \leqslant R^{-2/13}$ there are three NSCs, and when $R^{-2/13} \leqslant k \ll 1$ there are two NSCs (see Cowley & Smith 1985). Thus, to understand the effect of crossflow in PCP flows, the different regimes of k need to be considered separately.

For $R_{inj} \approx 0$, we expect the stability behaviour to be close to that of the PCP flow without crossflow. Intuitively, we expect the crossflow to stabilize, and so study the range $c_{r,crit} < k \leqslant k_1(R_{inj}=0)$. We examine the NSCs obtained from the O-S equation corresponding to $k=0.5$, under different values of R_{inj}; see figure 7(a). As expected, increasing R_{inj} results in a progressively larger critical $R=R_{crit}$. We also observe that both the upper and lower branches are oriented at an angle of 45° (i.e. $\alpha \sim R^{-1}$) at high values of R. On fixing R_{inj} and increasing k we have found that for successively larger k the upper and lower branches move together as R_{crit} increases, eventually coalescing at $k=k_1(R_{inj})$. This mechanism is identical with that observed by Cowley & Smith (1985), suggesting the applicability of a long-wavelength approximation in order to predict $k_1(R_{inj})$. Figure 7(b) plots the values of c_r at criticality, as R_{inj} is varied, also for $k=0.5$. The critical values are tabulated in table 1. The dependence is initially linear. We observe that $k > c_{r,crit}$ over the computed range.

3.1. *Long-wavelength approximation*

We follow the long-wavelength distinguished limit approach of Cowley & Smith (1985), taking $\alpha \to 0$ and $R \to \infty$, with $\lambda=(\alpha R)^{-1}$ fixed. The product αR is fixed along the upper and lower branches of the NSC. Thus, as the two branches of the NSC coalesce, in the (k,λ)-plane we observe $k \to k_1(R_{inj})$. In the long-wavelength

R_{inj}	α_{crit}	R_{crit}	$c_{r,crit}$
0	0.3851	22600	0.2344
0.1	0.3576	22538	0.2370
0.2	0.3275	22924	0.2394
0.3	0.2950	23986	0.2415
0.4	0.2550	26321	0.2433
0.5	0.2000	31656	0.2452
0.6	0.1200	51115	0.2461

TABLE 1. Critical values for $k=0.5$ and increasing R_{inj}.

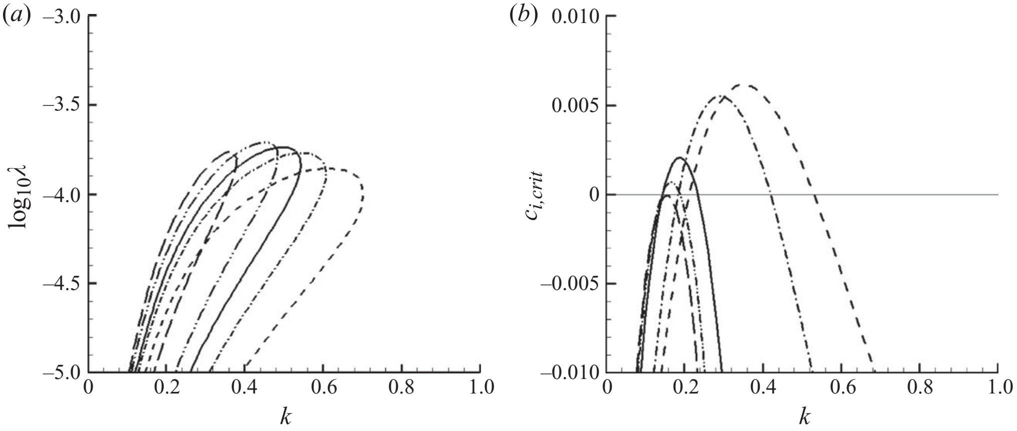

FIGURE 8. (*a*) Long-wave NSCs showing the dependence of λ on k for $R_{inj}=0$ (– – –), 0.3 (– · –), 0.5 (——), 0.7 (–··–) and 1 (— —); (*b*) $c_{i,crit}$ versus k for $\lambda=2.5\times10^{-5}$, and $R_{inj}=0$ (– – –), 0.3 (– · –), 1 (——), 1.2 (–··–) and 1.3 (— —).

limit, (2.16) becomes

$$\mathrm{i}\lambda\left[\mathrm{D}^4-R_{inj}\mathrm{D}^3\right]\phi+(u-c)\,\mathrm{D}^2\phi-(\mathrm{D}^2u)\phi=0, \tag{3.1}$$

with boundary conditions (2.17).

Figure 8(*a*) shows the NSC obtained from (3.1), plotted in the (k,λ)-plane for various R_{inj}. The cutoff value $k_1(R_{inj})$ is the maximal value of k on each of these curves. These values are listed in table 2. We also list the dimensionless wall speeds at cutoff, i.e. $\tilde{k}(k_1, R_{inj})$. We observe that the cutoff wall speed decreases with R_{inj}. This is in agreement with the concluding remarks of § 2.3.3.

Figure 8(*b*) shows c_i for the least stable eigenvalue of the long-wavelength problem, for fixed $\lambda=2.5\times10^{-5}$ and different values of R_{inj}, as k is varied. When $R_{inj}\geqslant1.3$, we find that $c_{i,crit}\leqslant0$, $\forall\ k\in(c_{r,crit},k_1(0)]$, implying that there are no neutral or unstable long-wavelength perturbations in this range of k (i.e. at least until we approach the second transition at $R_{inj,2}$). Thus, in this initial range of say $R_{inj}\lesssim1.3$, provided that $k>c_{r,crit}$, we can talk equally of a cutoff value for k or for R_{inj}.

3.2. *Effects of asymmetry of the velocity profile*

We observe that R_{inj} enters the stability problem in two distinct ways. The first one represents the direct contribution of the additional third-order inertial term, $R_{inj}\mathrm{D}(\alpha^2-\mathrm{D}^2)\phi$, in the O-S equation (2.16). For the second one, R_{inj} influences the

$R_{inj,1}$	k_1	$c_{r,crit}$	$\tilde{k}(k_1, R_{inj,1})$
0	0.70	0.2331	0.5070
0.3	0.60	0.2431	0.4657
0.5	0.54	0.2455	0.4386
0.7	0.48	0.2472	0.4085
1.0	0.38	0.2358	0.3489
1.29	0.19	0.1556	0.1939

TABLE 2. Cutoff values k_1 and wave speed $c_{r,crit}$ for increasing R_{inj}.

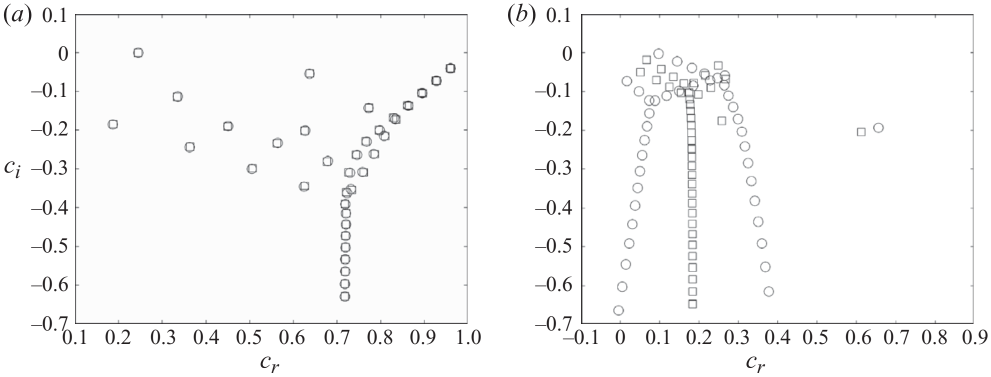

FIGURE 9. Eigenspectrum for $(k, \alpha, R) = (0.5, 0.2, 31656)$: (*a*) $R_{inj} = 0.5$ (critical conditions) and (*b*) $R_{inj} = 23.5$. Symbols: ○, the eigenspectrum from the O-S equation; □, the spectrum obtained by neglecting the additional crossflow inertial term.

base velocity profile. To explore which of these effects is dominant, we show in figure 9 the spectra of (2.16) and (2.17) obtained with and without the term $R_{inj}\mathrm{D}(\alpha^2 - \mathrm{D}^2)\phi$ included in the computation. The critical parameters corresponding to $R_{inj} = 0.5$, in table 1, are chosen and fixed for this comparison. Figure 9(*a*) shows the two spectra at $R_{inj} = 0.5$, which are near identical, completely overlapping on the figure. This suggests that at smaller R_{inj}, the effects of crossflow are manifested completely via the base flow velocity profile. Figure 9(*b*) shows a similar comparative study at a larger value of R_{inj}, closer to $R_{inj,2}$. In this figure, we see a distinct difference between the spectra. The additional third-order term is apparently responsible for the splitting of the A, P and S families illustrated in figure 4(*b*).

In figure 10, we plot k_1 against $R_{inj}(= R_{inj,1})$. A linear dependence is evident. The slope of the line is approximately $-1/3$. The flow is unconditionally linearly stable above the line and conditionally unstable otherwise. For small values of R_{inj}, we have seen in figure 1 that the principal effect is to skew the velocity profile towards the upper wall. A similar asymmetric skewing of the velocity profile is also induced in an ACP flow, through geometric means by varying the radius ratio η (defined as the radius of the outer stationary cylinder to the radius of inner moving cylinder). ACP flow has been studied extensively by Sadeghi & Higgins (1991), and we superimpose their results on ours, in figure 10. The comparison is striking. We believe there are two features of figure 10 that are unusual and worthy of note. Unsurprising is of course the identical limits $R_{inj} = 0 = (\eta - 1)$. Note that $R_{inj} \to 0$ is the PCP flow, and $\eta \to 1$ represents the narrow gap limit of ACP, which is also the PCP flow.

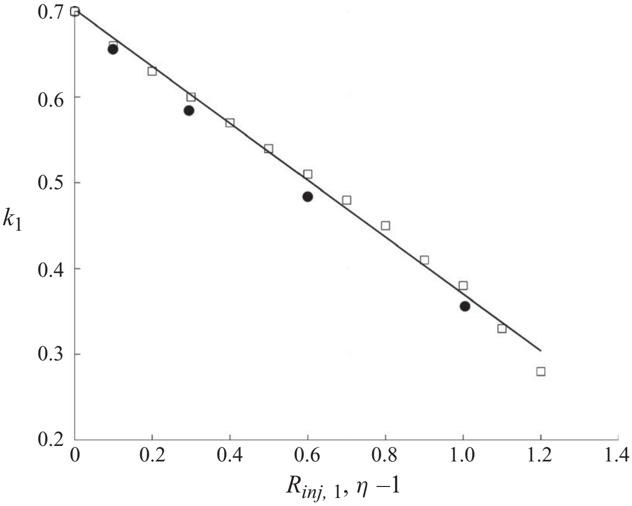

FIGURE 10. k_1 as a function of $R_{inj,1}$ (□) as well as the radius ratio η (●) in ACP flow (Sadeghi & Higgins 1991).

The first feature is the very similar linear decay in critical $k = k_1(R_{inj})$, from the PCP values. It can be argued along the lines of Mott & Joseph (1968) that for a fixed Couette component (k), increasing the crossflow for the PCP flow, or the radius ratio in the ACP flow of Sadeghi & Higgins (1991), skews the velocity profile more towards the moving boundary, thus increasing asymmetry and thereby stability. Because it has been observed in figure 9(a) that for small R_{inj} the influence of injection on the eigenspectrum is through the velocity profile only, we do expect stabilization. However, when $(\eta - 1)$ and R_{inj} are $O(1)$, we can see no obvious quantitative relation between these flows and even the stability operators are quite different.

The second noteworthy feature of figure 10 is that there is a minimum value of k_1 ($k_{1,min}$) below which it is not possible to produce unconditional stability by applying (modest) crossflow. This minimum value is found when $k_1 \rightarrow c_{r,crit}$. We have found approximately that $k_{1,min} = 0.19$ and the corresponding $R_{inj,1} = 1.29$. This is very similar to Sadeghi & Higgins (1991), who found that the critical layer near the moving wall of ACP flows remained up to $c_{r,crit} \approx 0.18$.

3.2.1. *Linear energy budget considerations*

The strong analogy with the ACP flow results of Sadeghi & Higgins (1991) suggests that a similar mechanism may be responsible for the stabilization and cutoff behaviour. To investigate this we examine the linear energy equation, derived in modal form from the Reynolds–Orr energy equation. This yields the following two identities:

$$c_i = \frac{\langle(\phi_r \mathrm{D}\phi_i - \phi_i \mathrm{D}\phi_r)\mathrm{D}u\rangle - \dfrac{1}{\alpha R}\left[I_2^2 + 2\alpha^2 I_1^2 + \alpha^4 I_0^2\right]}{I_1^2 + \alpha^2 I_0^2}, \tag{3.2}$$

$$c_r = \frac{\langle(\alpha^2|\phi|^2 + |\mathrm{D}\phi|^2)u\rangle + \dfrac{R_{inj}}{\alpha R}\langle\alpha^2(\phi_r \mathrm{D}\phi_i - \phi_i \mathrm{D}\phi_r) + (\mathrm{D}\phi_r \mathrm{D}^2\phi_i - \mathrm{D}\phi_i \mathrm{D}^2\phi_r)\rangle}{I_1^2 + \alpha^2 I_0^2}, \tag{3.3}$$

where $I_k = I_k(\phi)$ is the semi-norm defined by

$$I_k = \left[\int_{-1}^{1} |\mathrm{D}^k \phi|^2 \, \mathrm{d}y \right]^{1/2}, \quad k = 0, 1, 2,$$

and where

$$\langle f \rangle = \int_{-1}^{1} f(y) \, \mathrm{d}y.$$

Before proceeding further, we note that R_{inj} only appears indirectly in (3.2), reinforcing the assertion that for order unity R_{inj}, the principal contribution to stability of injection is via the mean flow. Indeed, in the long-wavelength limits of cutoff k that we have studied, we have found values $\lambda = (\alpha R)^{-1} \lesssim 10^{-4}$ for instability. Thus, in (3.3) the term directly involving R_{inj} has minimal effect on c_r, explaining the observations in figure 9(*a*).

The identity (3.2) can also be interpreted as an energy equation, in the form:

$$\frac{\mathrm{d}}{\mathrm{d}t} \langle T_1 \rangle = \langle T_2 \rangle - \frac{1}{R} \langle T_3 \rangle, \tag{3.4}$$

where

$$T_1 = 0.5(|\mathrm{D}\phi|^2 + \alpha^2 |\phi|^2), \qquad \frac{\mathrm{d}}{\mathrm{d}t} T_1 = \alpha c_i T_1, \tag{3.5}$$

$$T_2 = 0.5 \alpha \tau \mathrm{D}u, \qquad \tau = \phi_r \mathrm{D}\phi_i - \phi_i \mathrm{D}\phi_r, \tag{3.6}$$

$$T_3 = 0.5(|\mathrm{D}^2\phi|^2 + 2\alpha^2 |\mathrm{D}\phi|^2 + \alpha^4 |\phi|^2). \tag{3.7}$$

The left-hand side of (3.4) represents the temporal variation of the spatially averaged (one wavelength) kinetic energy. The first term on the right-hand side of (3.4) is the exchange of energy between the base flow and the disturbance. The last term, $(\langle T_3 \rangle / R)$, represents the rate of viscous dissipation. At criticality, the two terms on the right-hand side balance each other, but the spatial distributions of T_2 and T_3/R indicate where the energy is generated and dissipated in the channel.

Sadeghi & Higgins (1991) extensively utilized this linear energy approach in studying the effect of k on the stability of ACP flow. They found that increase in the value of $k - c_{r,crit}$ decreases the Reynolds stress (τ) near the moving wall until it becomes negative, hence stabilizing. The critical layer near the moving wall vanishes for $k > c_{r,crit}$, and as k increases the Reynolds stress becomes progressively negative within the critical layer at the fixed wall, but this behaviour is destabilizing because the velocity gradient is negative there for ACP flow.

Figure 11(*a–d*) examines the distribution of T_2 and T_3/R for the least stable eigenmode for the parameters listed in table 1, i.e. we fix $k = 0.5$ and increase R_{inj} up to $R_{inj} = R_{inj,1} \approx 0.6$. The critical layer is marked with a vertical line. We observe that both the rate of energy transfer and the rate of viscous dissipation decrease with the crossflow. Without crossflow, T_2 is positive and negative respectively in the lower (injection) and upper (suction) halves of the domain. Increasing the crossflow decreases both the positive (near injection wall) and negative (near suction wall) peaks. The location of the critical layer also moves away from the injection wall because of the skewing of the velocity profile. When $R_{inj} \approx R_{inj,1}$, $\langle T_2 \rangle$ and $\langle T_3 \rangle / R$ not only equalize but (because ϕ has been normalized) will have magnitudes $O(\alpha^{-1})$ because $\alpha R =$ constant at cutoff (see also Sadeghi & Higgins 1991). This reduces the energy budget as $R_{inj} \approx R_{inj,1}$, and is the primary reason for the cutoff.

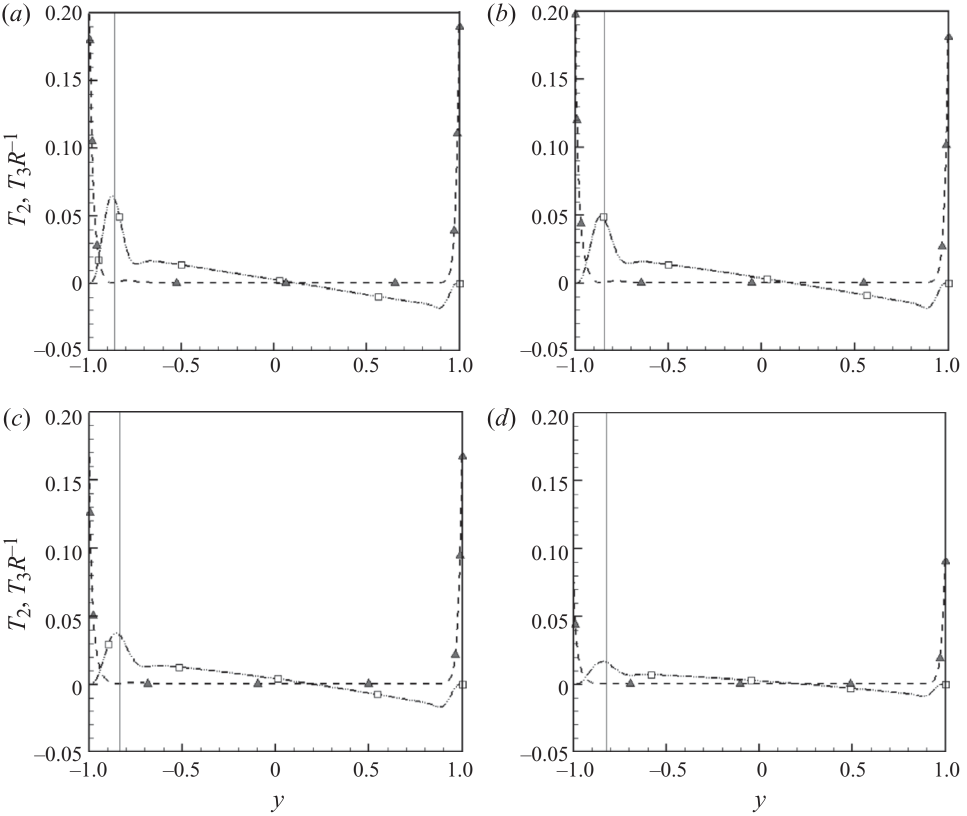

FIGURE 11. Distribution of energy production (T_2) and dissipation (T_3/R) terms across the domain corresponding to criticality at R_{inj} = (*a*) 0, (*b*) 0.2, (*c*) 0.4 and (*d*) 0.6. In all the cases, $k = 0.5$. Symbols: ··–□–··, T_2; –▲–, T_3/R. The solid vertical line represents the location of the critical layer.

3.3. *Summary*

For the range of small to order unity R_{inj} with $k \geqslant c_{r,crit}$, the flow instability is dominated by long-wavelength perturbations. This instability mechanism exhibits a cutoff phenomenon characterized by a near linear boundary in the (R_{inj}, k)-plane. The initial cutoff mechanism is very similar to that for ACP, as studied by Sadeghi & Higgins (1991), combining skewing of the velocity profile, shifting of the critical layer and decay of the net perturbation energy.

4. Intermediate R_{inj} and short-wavelength instabilities

We now consider the range $0 \leqslant k \leqslant c_{r,crit}$, in which the critical layer at the upper wall is still present. We investigate its stability characteristics by adding crossflow of intermediate strength ($0 \leqslant R_{inj} \lesssim 21$), avoiding for the moment the second transition. It is intuitive that the presence of the critical layer will affect the stability behaviour. To verify this we have studied the two extremities of the range of k considered, i.e. $k = 0$ (PP flow) and $k = 0.18$. The respective NSCs are shown in figure 12. It is evident that the presence of the critical layers renders shorter wavelength modes unstable. Yet, also with R_{inj} in this intermediate range, the stability increases dramatically.

k_1	$R_{inj,1}$	α_{crit}
0	20.8	3.5227
0.0225	20.6	3.7458
0.0450	20.0	3.9381
0.0675	18.6	3.9831
0.0900	15.6	3.4146
0.1125	14.4	3.2112
0.1350	13.4	3.2112
0.1575	12.6	3.2112
0.1800	11.8	3.2112

TABLE 3. Cutoff values evaluated for shorter wavelength instabilities for $R = 10^6$.

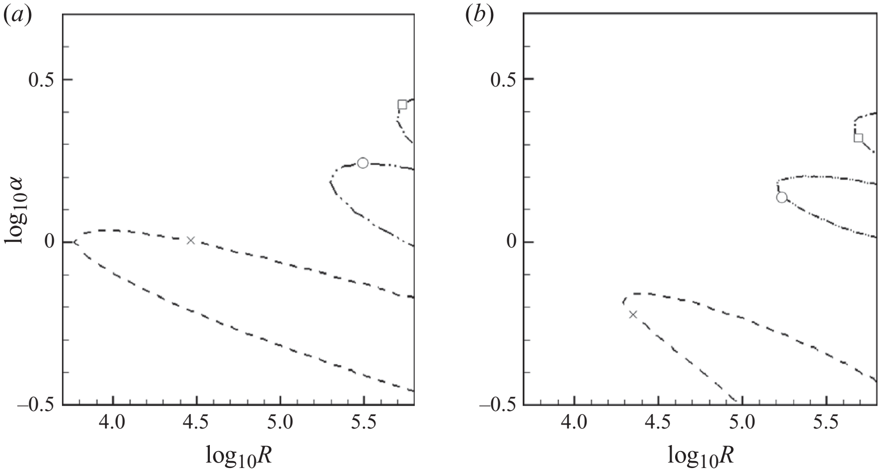

FIGURE 12. NSCs for (a) $k = 0$ and (b) 0.18 at different R_{inj}. The symbols, which indicate different values of R_{inj}, are as follows: ×, $R_{inj} = 0$; ○, $R_{inj} = 6$ in (a) and 4 in (b); □, $R_{inj} = 12$ in (a) and 8 in (b).

We have been unable to make any advance analytically in this range of R_{inj}, and therefore have proceeded numerically. First, when we considered $k \gtrsim 0.19$ for the range of $1.3 < R_{inj} < 21$, we found that the least stable modes are long-wavelength modes and that these are linearly stable. Thus, $k \gtrsim 0.19$ appears to represent an absolute cutoff in this range of R_{inj}.

For smaller k, we have seen that the NSCs occur with wavenumbers that are $O(1)$ and apparently increasing with R_{inj}. Unlike the long-wavelength problem, the asymptotic behaviour along the branches of the NSCs is not easily treated. At fixed large R, we are able to compute numerically a cutoff value of k for increasing R_{inj}, i.e. $k = k_1(R_{inj}, R)$. These cutoff curves do lie below $k \sim 0.19$, but are not wholly independent of R, at least within the range of R up to which our numerical code is reliable, i.e. it is quite possible that these asymptote to a cutoff curve as $R \to \infty$, but we cannot reliably evaluate this limit numerically. As an example of this numerical cutoff (at $R = 10^6$), we have computed the cutoff values $R_{inj,1}$, as listed in table 3 and shown in figure 13(a). For the range $1.4 < R_{inj} < 11.8$, the cutoff is close to $k \sim 0.19$.

Although we see that the unstable wavenumbers increase with R_{inj} in figure 12, note that asymptotically as $\alpha \to \infty$ the short wavelengths are stable. To see this, from

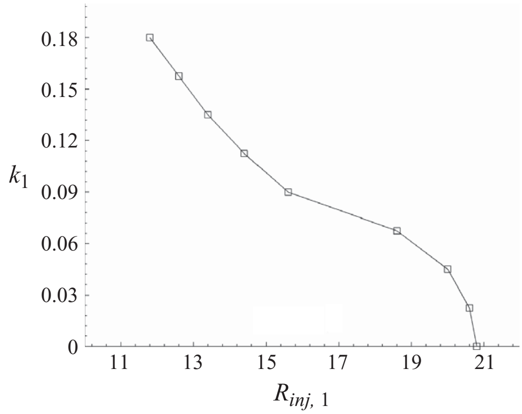

FIGURE 13. Shorter wavelength cutoff showing k_1 as a function of $R_{inj,1}$. The flow is linearly stable for $R \leqslant 10^6$ above the curve. The values in table 3 are marked by □.

(3.2) we bound

$$\langle(\phi_r \mathrm{D}\phi_i - \phi_i \mathrm{D}\phi_r)\mathrm{D}u\rangle \leqslant |\mathrm{D}u|_{max} I_0 I_1 \leqslant 0.5 |\mathrm{D}u|_{max} [\alpha I_0^2 + I_1^2/\alpha],$$

so that $c_i < 0$ provided that

$$R < \frac{|\mathrm{D}u|_{max}}{2\alpha^2} \tag{4.1}$$

(and better bounds are certainly possible). In table 3 the maximal critical wavenumber is in fact attained at an intermediate R_{inj}.

4.1. *Behaviour of preferred modes for intermediate R_{inj}.*

In our preliminary results in § 2.3, we saw that at fixed values of (R, k, α), increasing R_{inj} led to regimes of stabilization, then destabilization, and finally stabilization. For $k \geqslant c_{r,crit}$, only long wavelengths appear unstable, and how the cutoff values of k and R_{inj} vary in this regime are illustrated in figure 10. For the lower range of k, our results are primarily numerical, indicating a cutoff value $k \approx 0.19$ for $1.3 \lesssim R_{inj} \lesssim 11.8$ and then with decaying cutoff k for $11.8 \lesssim R_{inj} \lesssim 20.8$, as illustrated in figure 13. Therefore, we have linear stability as we cross some cutoff frontier, $k > k_1(R_{inj})$ in the (R_{inj}, k)-plane (alternatively for $R_{inj} > R_{inj,1}$).

We now consider what happens to the certain eigenmodes (preferred modes) as we extend the injection crossflow up until the second critical R_{inj}. Our analysis up to now suggests that the behaviour may be different depending on whether we consider small or moderate k. In figure 14, we have plotted the locations of certain eigenmodes as R_{inj} is increased, by keeping the Reynolds number, R, constant at 10^6. This gives us some idea of how cutoff behaviour changes with R_{inj}. Although the 'preferred modes' are simply those we have selected, we implicitly mean modes that are involved in the transition from stable to unstable as one of our dimensionless parameters is varied (here R_{inj}), i.e. at some point a preferred mode becomes the least stable mode and then unstable.

Figure 14(a) shows two eigenmodes corresponding to $k = 0$ (PP flow). A least stable long-wavelength mode is tracked for $\alpha = 0.001$, denoted by A. This mode is stable at $R_{inj} = 0$ and its stability increases further as R_{inj} increases up to around 1.7. However, further increases in R_{inj} destabilize this mode progressively until it becomes unstable at $R_{inj} = 25$. In the inset of figure 14(a) we have also plotted the least stable

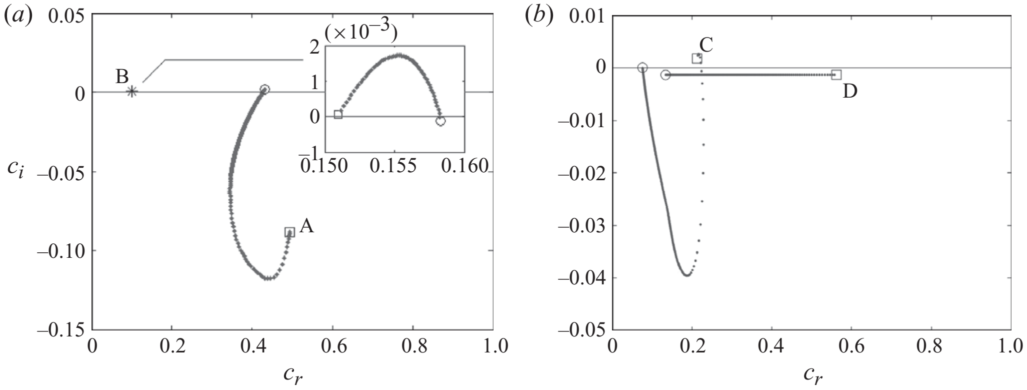

FIGURE 14. Behaviour of preferred modes (belonging to different wavelengths and denoted by letters A–D) under the influence of crossflow with $R = 10^6$. Symbols □ and ○ respectively imply the starting and the ending position of the preferred mode in the c_i, c_r plane, whereas the dots ('.') trace the locus. The difference in R_{inj} between consecutive dots is 0.1. (*a*) $k = 0$. Mode A has $\alpha = 0.001$ and is traced for $R_{inj} = [0,25]$. Mode B has $\alpha = 3.5227$ and is traced for $R_{inj} = [15, 21]$ (shown in the inset), the position at $R_{inj} = 15$ is marked by '$*$'. (*b*) $k = 0.5$. Mode C has $\alpha = 0.01$ and is traced for $R_{inj} = [0,30]$. Mode D has $\alpha = 2.5$ and is traced for $R_{inj} = [7,30]$.

short-wavelength mode at $\alpha = 3.5227$. Such modes become unstable only under the influence of crossflow of intermediate strength. This particular mode (denoted by B) starts becoming unstable approximately when $R_{inj} > 15$, but recovers stability later for $R_{inj} \geqslant 20.8$. This behaviour is a direct consequence of the trajectory of the NSCs observed in figure 12(*a*). The preferred mode B is the critical mode at cutoff (see table 3). Thus, PP flow with crossflow is unconditionally linearly stable in the range $20.8 \leqslant R_{inj} \lesssim 25$.

For larger k, the stability behaviour is primarily governed by the long-wavelength modes, as shown in figure 14(*b*) for $k = 0.5$. The least stable mode corresponding to $\alpha = 0.01$ is unstable for $R_{inj} = 0$, denoted mode C. This viscous mode becomes stable when R_{inj} increases to 0.6, which is indeed the cutoff value, i.e. $R_{inj,1}$. This is expected according to table 2. Mode C is weakly damped and its stability increases for $R_{inj} \lesssim 3$, after which it starts destabilizing. The mechanism of this destabilization can probably be analysed along the lines of resonant interactions of the T-S waves (see Baines *et al.* 1996). To show this interaction, we have traced the locus (for $R_{inj} = [7, 30]$) of the least stable inviscid short-wavelength mode D at $\alpha = 2.5$. This mode, being inviscid, remains stable but has c_i very close to zero as R_{inj} increases. The wave speed c_r decreases continuously with R_{inj} for mode D. The resonant interaction takes place when its wave speed matches that of mode C, which signals the destabilization of mode C. This destabilization continues until mode C becomes unstable when $R_{inj} \gtrsim 30$.

In figure 15 we show examples of the streamfunction for the preferred modes, corresponding to various k and R_{inj} in the transitions of figure 14. For the long-wavelength mode C, figure 15(*a–c*) shows that strong R_{inj} appears to skew the streamlines towards the lower wall. The same is true for the long-wavelength mode A under strong injection; see figure 15(*f*). On the contrary, figure 15(*d*,*e*) shows that for large R_{inj}, the streamlines of the shorter wavelength mode B are skewed and localized towards the upper wall.

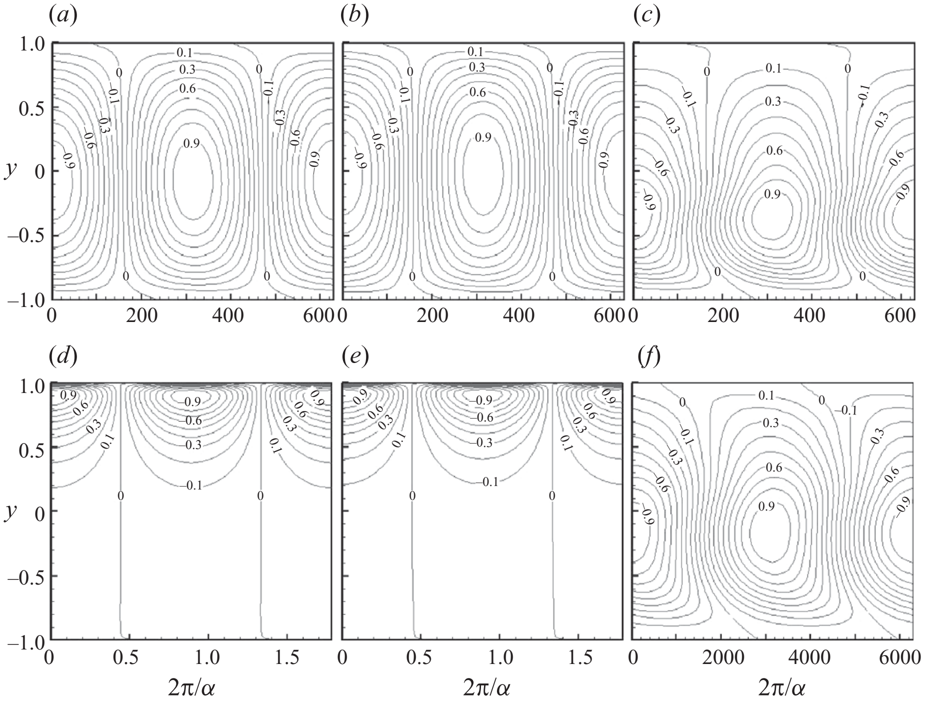

FIGURE 15. Isovalues of the normalized perturbation streamfunctions ($\hat{\psi}$) for the preferred modes at $R = 10^6$ under different R_{inj}. The streamwise extent of the domain is one wavelength. Corresponding to $k = 0.5$, the long-wavelength mode C is shown for (*a*) $R_{inj} = 0.1$ (unstable), (*b*) $R_{inj} = 1$ (stable) and (*c*) $R_{inj} = 30$ (unstable). Corresponding to $k = 0$, $\hat{\psi}$ for two different preferred modes, viz. A and B, are shown. The shorter wavelength mode B ($\alpha = 3.5227$) is shown for (*d*) $R_{inj} = 15$ (unstable) and (*e*) $R_{inj} = 21$ (stable). The longer wavelength mode A ($\alpha = 0.001$) is shown for (*f*) $R_{inj} = 25$ (unstable).

5. Stability and instability at large R_{inj}

We now turn to the transition to instability at $R_{inj,2}$ and later to stabilizing effects at very large R_{inj}. As observed in § 2.3, the transition at $R_{inj,2}$ appears to be independent of streamwise Reynolds number R (see figure 5*b*) and occurs for all k. Although there is sensitivity to k, it is not very significant. Values of $R_{inj,2}$ are found for all $k \in [0, 1]$ and are in a fairly tight range of $R_{inj} \sim 22$–25.

As suggested in the previous subsection, although instability at moderate R_{inj} may be either short wavelength or long wavelength, according to $(k - c_{r,crit})$, as we approach $R_{inj,2}$ from below it is the long wavelengths that are unstable. Figure 16(*a*) shows the neutral stability curves corresponding to PP flow for R_{inj} just above $R_{inj,2}$. The NSCs are nested with decreasing R_{inj}, and as we approach $R_{inj,2}$ the upper and lower branches of the NSC are seen to coalesce. The slope of the two branches suggests that $\alpha \sim R^{-1}$ in the limit of cutoff, and hence the previous long-wavelength approximation, leading to (3.1), should be effective for predicting the cutoff in the (k, λ)-plane (recall $\lambda = (\alpha R)^{-1}$).

Figure 16(*b*) shows the NSCs obtained from long-wave approximation. The cutoff velocity k_2 is the maximum value of k encountered along the NSC for a given $R_{inj} = R_{inj,2}$. Unlike figure 8, the entire range of k becomes unconditionally stable. For $R_{inj,1} < R_{inj} < 22.2$, $c_i < 0 \forall\ k \in [0, 1]$. Another significant difference with figure 8 and

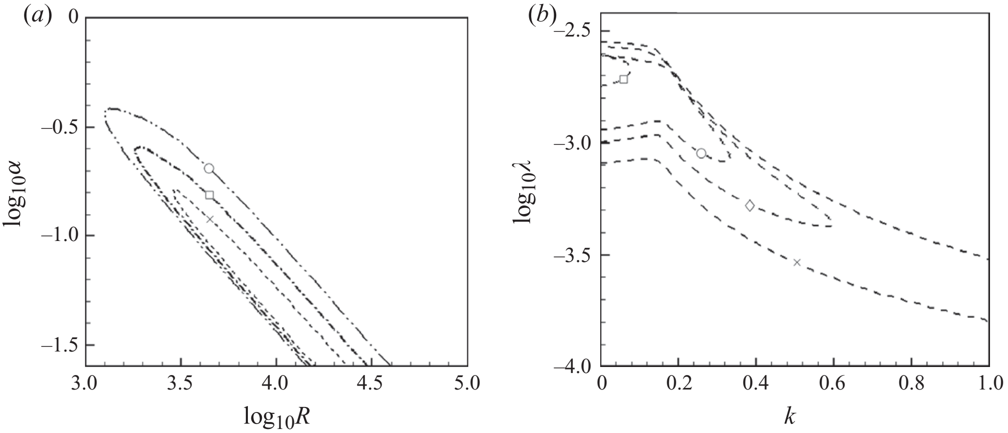

FIGURE 16. (a) NSC of PP flow ($k = 0$) when $R_{inj} \rightarrow R^{-}_{inj,2}$. The different values of R_{inj} are 22.5 (−×−), 23 (−·□·−) and 24 (−·○·−). Near cutoff, αR is constant along the upper and lower branches. (b) Long-wave NSCs showing the dependence of $\log_{10}\lambda$ on k. The different values of R_{inj} are 22.4 (□), 23.5 (○), 24 (◇) and 25 (×). Cutoff is achieved over the entire range of k, i.e. [0, 1].

the results of Cowley & Smith (1985) is that 'bifurcation from infinity' is not observed as $k \rightarrow 0$. This is possibly because the curves bifurcate from infinity for negative values of k, but we have not studied this range. Finally, for crossflow rates slightly greater than $R_{inj,2}$, the R_{crit} is relatively low for the entire range of k. For example, $R_{inj,2} \approx 23.8$ for $k = 0.5$ (implying $R_{crit} \rightarrow \infty$ as $R_{inj} \rightarrow R^{-}_{inj,2}$). Increasing R_{inj} to 25 decreases R_{crit} to around 6000. Thus, on crossing $R_{inj,2}$ we find a dramatic decrease in the flow stability.

5.1. *Linear energy balance at* $R_{inj,2}$

An interesting feature of transition at $R_{inj,2}$ is the independence with respect to R. With reference to the energy equation (3.4), this insensitivity implies that in this range $|T_2|$ is much larger than the viscous dissipation, T_3/R. In other words, at criticality $c_i = 0$ is achieved by a balance of energy production and dissipation within T_2, more so than via balance with the viscous dissipation. Figure 17(a) investigates the energy budget at criticality for $k = 0.5$ at $R_{inj} = 25$. The critical parameters are observed to be $(\alpha_{crit}, R_{crit}) = (0.31, 6000)$. This implies that on crossing the cutoff $R_{inj,2}$, there is a transition from unconditional stability ($R_{crit} \rightarrow \infty$) to high instability ($R_{crit} = 6000$). Comparing with figure 11 (which shows energy distribution corresponding to criticality for $k = 0.5$ and $R_{inj} \leqslant R_{inj,1}$), it is obvious that T_2 has a higher amplitude while the viscous dissipation T_3/R is weaker.

This behaviour is due to the generation of larger Reynolds stresses τ, as R_{inj} increases, as illustrated in figure 17(b). The dominance of T_2 over the viscous dissipation suggests that the critical layers have little to do with instability in this range. Note that τ is small in the critical layer, which has now moved towards the channel centre, and hence T_2 is also small. Referring to figure 2(b), the vanishing vorticity gradient (D^2u) found in the bulk of the flow domain at high values of R_{inj} removes/diminishes the singular effects associated with the critical layer.

The growth of τ is probably not responsible for the spreading of the spectrum along the real axis, which we have observed in figure 4(b). Equation (3.3) may be

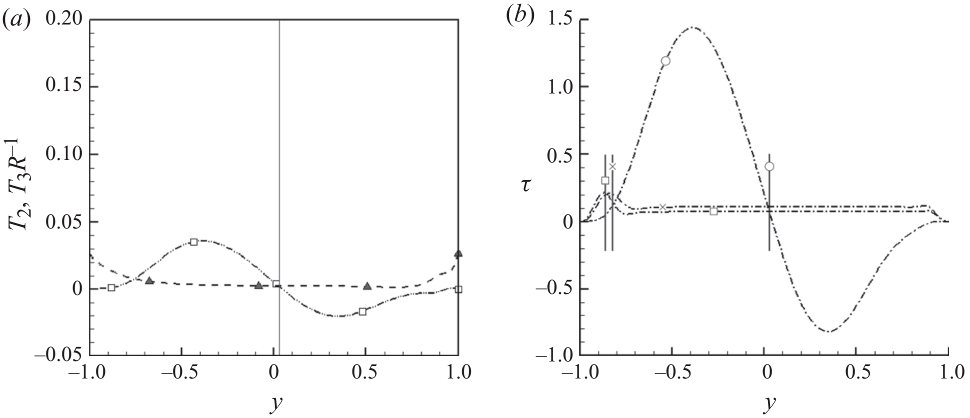

FIGURE 17. (*a*) Distribution of energy production (T_2) and dissipation (T_3/R) terms across the domain corresponding to criticality at $R_{inj}=25$. Symbols: –·□·–, T_2; –▲–, T_3/R. The solid vertical line represents the location of the critical layer. (*b*) Reynolds stress τ distribution at criticality for $R_{inj}=0$ (□), $R_{inj}=0.6$ (×) and $R_{inj}=25$ (○). The location of the critical layers is shown by solid lines with corresponding symbols.

rewritten as

$$c_r = \frac{\langle(\alpha^2|\phi|^2+|\mathrm{D}\phi|^2)u\rangle + \dfrac{R_{inj}}{\alpha R}\langle\alpha^2\tau - \phi_r\mathrm{D}^3\phi_i + \phi_i\mathrm{D}^3\phi_r\rangle}{I_1^2+\alpha^2 I_0^2}. \tag{5.1}$$

The first term leads simply to values of c_r in the range of u. The second term does contain $\alpha^2\tau$, i.e. longitudinal gradients of the Reynolds stresses. However, note that even for the shorter wavelengths we have $\alpha \sim O(1)$, and if we consider long wavelengths, we have typically found instability only for $\alpha R \gg 1$. Thus, even for these larger R_{inj}, the term involving $\alpha^2\tau$ is likely to be insignificant.

The extension of c_r beyond the usual bounds of the base flow velocity is therefore due to the third derivative terms in (5.1), which cannot be bounded by the denominator. Interestingly, therefore, the larger values of c_r, which indicate less regular eigenmodes, also lead to larger viscous dissipation, and hence more stable modes. This explains the shape of the spectrum in figure 4(*b*).

In figure 14(*b*), we tracked the behaviour of mode C as R_{inj} increased. This mode becomes unstable for $R_{inj} \geqslant R_{inj,2}$, implying that it governs the transition behaviour. In figure 18, we show the evolution of the energy balance terms for this mode as R_{inj} increases from zero. This mode is stable from $R_{inj}=0.6$ to 30. The cutoff achieved at $R_{inj}=0.6$ is primarily due to the increased viscous dissipation at both walls. This phenomenon continues until $R_{inj}\approx 3$; see figure 18(*d*). At this point, the 'viscous hump' observed near the lower wall gets amplified. This mechanism is probably due to the resonant interaction between mode C and an (approximately) neutrally stable inviscid mode, for example mode D. Further increase in R_{inj} thins out the viscous layer at the suction wall faster than that at the injection wall. Suction negates both the exchange and the dissipation of energy, and the viscous hump is localized within the lower half of the channel, i.e. injection side. Note that T_3/R reduces faster than T_2 and finally the mode becomes unstable when R_{inj} increases to 30. The condition at this point is $\langle T_2\rangle > (\langle T_3\rangle/R)$; see figure 18(*f*). Interestingly, the mode becomes unstable when the viscous hump reaches the centre of the channel. Further increase of R_{inj} results in a gradual reduction of T_2 and the mode becomes stable again. The

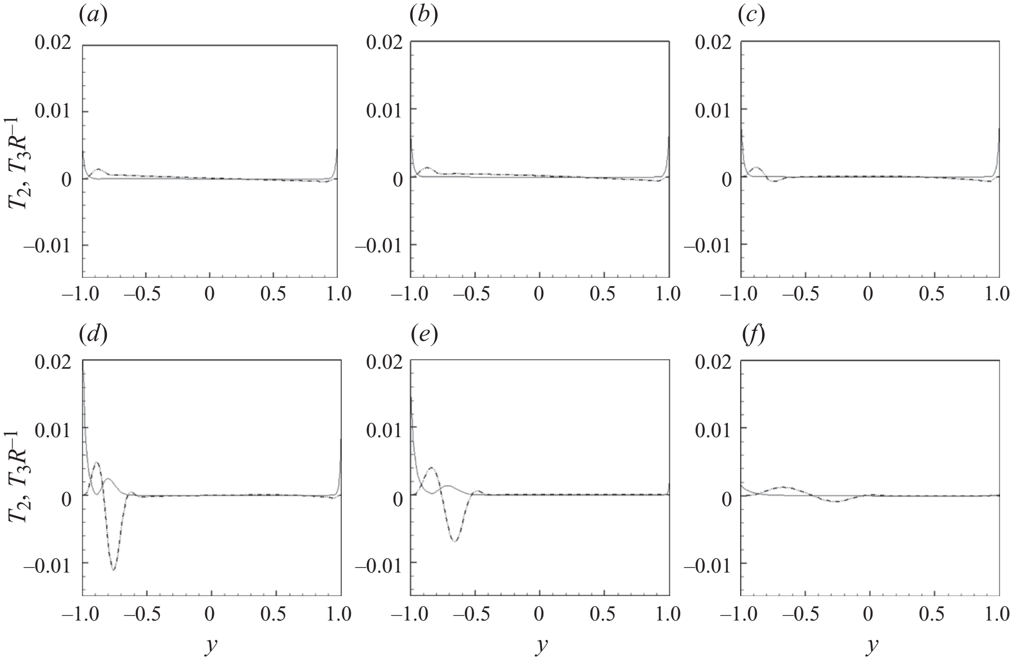

FIGURE 18. Distribution of energy production (T_2) and dissipation (T_3/R) terms across the domain corresponding to mode C at $R_{inj} =$ (*a*) 0, (*b*) 0.6, (*c*) 1, (*d*) 3, (*e*) 10 and (*f*) 30. The dash-dotted line represents T_2 and the solid line represents T_3/R.

mean perturbation kinetic energy $q(y)$ distribution provides further insight into the instability mechanism. It is defined modally to be

$$q = \tfrac{1}{4}\left(|D\phi|^2 + \alpha^2|\phi|^2\right). \tag{5.2}$$

Figure 19 shows the mean perturbation kinetic energy profiles for mode C at different R_{inj}. Each distribution of q has been normalized by its maximum value.

Without any crossflow, the amount of energy in the two halves of the domain is comparable, the suction half having ∼43 % of the energy (note $k = 0.5$). Increasing crossflow up to $R_{inj} \approx R_{inj,1} = 0.6$ increases the secondary peak until the cutoff is achieved. The energy in the suction half at this point is 46.7 %. The primary peak moves towards the lower wall but cannot reach it because of the no-slip conditions. At $R_{inj} > 1$, the primary peak starts moving away from the suction wall. At $R_{inj} = 3$, the mode is at its maximum stability (see figure 14*b*). At this point, the perturbation energy is highly localized within the lower one-eighth of the channel, along with a small secondary peak at the upper quarter. Further increase of R_{inj} to 10 causes the secondary peak to vanish; the energy content in the suction half being only ∼7.6 %. The resonant interactions of T-S waves result in the development of a secondary peak from the primary peak itself. During this process, the secondary peak slowly separates from the primary peak and moves in the direction of the upper wall. For $R_{inj} = 30$, the perturbation reaches the channel centre and the mode becomes unstable. The amount of energy in the suction half increases to 18.1 %. For even higher values of R_{inj}, for example 45, the upper half holds ∼32 % of the energy.

Thus, it appears that the onset of the cutoff at $R_{inj,1}$ occurs when the secondary peak holds maximum energy. Increasing injection decays this peak until it reaches a

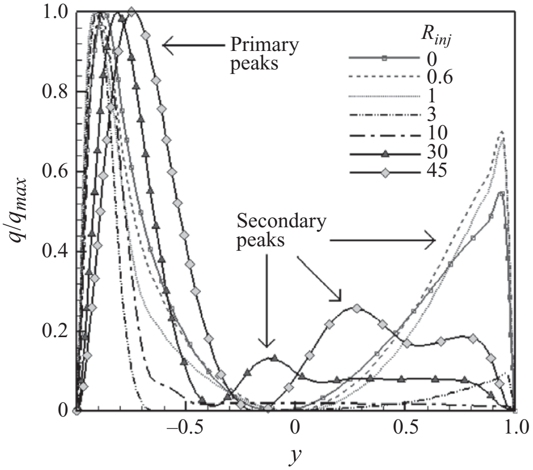

FIGURE 19. Non-dimensional mean perturbation kinetic energy profiles for mode C at different R_{inj}. Solid lines with symbols denote the unstable modes. For each R_{inj}, q has been scaled by its maximum value.

minimum and then starts to grow out from the primary peak. The end of the cutoff regime, marked by $R_{inj} > R_{inj,2}$, occurs when the secondary peak reaches the channel centre and holds sufficient energy.

5.2. *Eventual stabilization at $R_{inj,3}$*

We have not studied in detail the eventual stabilization of the flow at very large R_{inj} (i.e. $R_{inj} \sim R_{inj,3}$), but we believe the energetics of this stabilization are due to a decay in the energy production. This can be seen most clearly from the identity (3.2), which is in the same form as that for any parallel shear flow, i.e. crossflow only influences (3.3) directly. Joseph has used this expression to derive general bounds that depend on $|\mathrm{D}u|_{max}$, and various functional inequalities; see Joseph (1968, 1969). For example, we have linear stability provided that

$$\alpha R|\mathrm{D}u|_{max} < \max(\xi^2\pi + 2^{3/2}\alpha^3, \xi^2\pi + \alpha^2\pi), \tag{5.3}$$

where $\xi = 2.36502$ is the least eigenvalue of a vibrating rod with clamped ends at $y = \pm 1$.

The condition (5.3) evidently holds for the flows we consider, but is very conservative and especially so in the limit of large R_{inj}. This conservatism at large R_{inj} stems directly from the simplistic treatment of $\mathrm{D}u$ in bounding the energy production term:

$$\langle(\phi_r \mathrm{D}\phi_i - \phi_i \mathrm{D}\phi_r)\mathrm{D}u\rangle < |\mathrm{D}u|_{max} I_0 I_1.$$

With reference to figures 1 and 2 and to (2.11), we see that at large R_{inj} the base velocity profile consists of a thin layer near the upper suction wall, within which $\mathrm{D}u \sim |\mathrm{D}u|_{max} \sim R_{inj}$, which has thickness of $O(R_{inj}^{-1})$. Away from this thin boundary layer, the velocity gradients are of size $\mathrm{D}u \sim 2(kR_{inj})^{-1} + O(R_{inj}\mathrm{e}^{-R_{inj}(1-y)})$. Note, however, that within this suction layer, we have $\phi \sim (1-y)^2$ due to the boundary conditions on the perturbation. Therefore, taking a nominal suction layer boundary at $y = y_s$, we may estimate as follows:

$$
\begin{aligned}
\langle(\phi_r \mathrm{D}\phi_i - \phi_i \mathrm{D}\phi_r)\mathrm{D}u\rangle &= \int_{-1}^{1-y_s} (\phi_r \mathrm{D}\phi_i - \phi_i \mathrm{D}\phi_r)\mathrm{D}u \,\mathrm{d}y + \int_{1-y_s}^{1} (\phi_r \mathrm{D}\phi_i - \phi_i \mathrm{D}\phi_r)\mathrm{D}u \,\mathrm{d}y \\
&\leqslant \frac{2}{kR_{inj}} \int_{-1}^{1-y_s} |\phi_r \mathrm{D}\phi_i - \phi_i \mathrm{D}\phi_r| \,\mathrm{d}y + O(|\mathrm{D}u|_{max}(1-y_s)^4) \\
&\leqslant \frac{2}{kR_{inj}} I_0 I_1 + O\left(R_{inj}^{-3}\right).
\end{aligned}
\tag{5.4}
$$

Following Joseph (1969), this leads directly to the bound

$$
\frac{2\alpha R}{kR_{inj}} \lesssim \max(\xi^2\pi + 2^{3/2}\alpha^3, \xi^2\pi + \alpha^2\pi), \tag{5.5}
$$

sufficient for linear stability at large R_{inj} (with asymptotically $kR_{inj} \gtrsim 4$ required). In other words, at large R_{inj}, the energy production T_2 will decay like $(kR_{inj})^{-1}$ at leading order, so that the viscous dissipation need only be of this order to stabilize the flow.

6. Summary

We have presented a detailed analysis of linear stability and instability in the (R_{inj}, k)-plane, for PCP flow with crossflow. The most complete analysis concerns the important range of low R_{inj} and modest k. In this range, we have demonstrated that the stabilization mechanism, due to either injection or wall motion, is essentially the same. Long wavelengths dominate. Skewing of the velocity profile shifts the critical layer and at the same time the energy production is diminished until viscous dissipation dominates at cutoff. In figure 10, we have also shown an interesting quantitative analogy with the cutoff behaviour of ACP flows; see Sadeghi & Higgins (1991).

This lower range of R_{inj} and modest k is probably that which is most important practically. Essentially, this range allows one to compensate crossflow by wall motion and vice versa, achieving unconditional linear stability via either mechanism. With reference to figure 1, it is the range of R_{inj} in which the crossflow and wall motion are modifications of a base Poiseuille flow. Because of the scaling, the peak velocity is always 1, but at larger R_{inj} with modest k, the Poiseuille component is completely dominated by crossflow and wall motion.

Globally, the cutoff regimes in the (R_{inj}, k)-plane are as illustrated in figure 20. The shaded area shows the region of unconditional linear stability. In the intermediate range of approximately $1.3 \leqslant R_{inj} \leqslant 20.8$, values of $k \gtrsim 0.19$ are dominated by long wavelengths and are stable. Below this value, we are able to compute numerical cutoff curves for fixed R. With the limits of our computations, we cannot determine if these cutoff curves asymptote to an unconditional cutoff curve as $R \rightarrow \infty$.

There appears to be a short band of unconditional linear stability for all computed values of k around approximately $20.8 \leqslant R_{inj} \leqslant 22$, before the destabilization occurs at larger $R_{inj} = R_{inj,2}$. Because this band can make PP flow unconditionally stable, it could be effectively used in applications where wall motion is not feasible, e.g. crossflow filtration, medical dialysis. From the practical perspective, the transition across $R_{inj,2}$ is from unconditional stability to critical values of R which are relatively modest (e.g. in the range 10^3–10^4), just a short distance beyond $R_{inj,2}$. Assuming that the PP flow is linearly unstable, this means that stabilization can be achieved with crossflow velocities of the order of 1 % of the mean axial flow velocity.

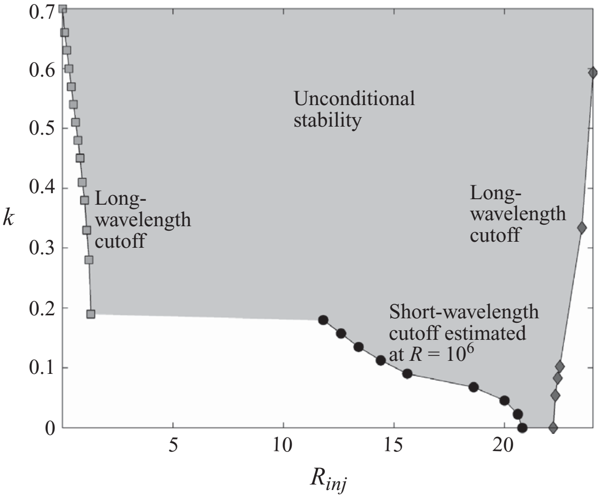

FIGURE 20. Variation of k with R_{inj}. Symbols: ▨, the long-wavelength cutoff achieved for $0.7 \geqslant k \geqslant 0.19$; ●, the shorter wavelength cutoff for $0.19 > k \geqslant 0$ evaluated numerically for $R = 10^6$; ◆, the second long-wavelength cutoff. The shaded region depicts the entire zone of unconditional linear stability.

This destabilization at $R_{inj,2}$ is again a long-wavelength mechanism, which we have analysed using the long-wavelength approximation of Cowley & Smith (1985). A possible cause of this instability has been found to be resonant interactions of the T-S waves. A study of the linear energetics of the upper limit, $R_{inj,2}$, has shown that neither viscous dissipation nor the involvement of a critical layer is significant. Rather, the balance of energy production and dissipation within T_2 keeps the mode neutrally stable. An energy analysis of the preferred mode C has revealed that the precursor of the transition to instability from unconditional stability is the amplification of disturbances near the injection wall. The mean perturbation kinetic energy has also been analysed. It has been shown that the lower limit occurs when the secondary peak holds maximum energy. Increasing injection decreases the secondary peak until it reaches a minimum and then it starts to grow from the primary peak. When the secondary peak reaches the channel centre and holds a sufficient amount of energy, the unconditional stability mechanism breaks down.

The final stabilization occurring at large $R_{inj} \geqslant R_{inj,3}$ has been analysed using linear energy bounds. By a careful treatment of the energy production term, we are able to show that the energy production terms decrease asymptotically like R_{inj}^{-1} as $R_{inj} \to \infty$. We believe that this mechanism leads to the eventual domination of the viscous dissipation at large enough R_{inj}.

In terms of the spatial structure of the perturbations, we note that the stabilizations at small and moderate R_{inj} are both long-wavelength phenomena for which the approximation of Cowley & Smith (1985) has been shown effective. Implicitly, therefore, the critical wavenumbers scale like R^{-1} in these limits. For the shorter wavelength instabilities, we have not analysed the asymptotic behaviour of the wavenumber with R. A more detailed look at the spatial structure of certain eigenmodes has been presented in figure 15. This shows a skewing of the streamline recirculatory regimes towards the lower wall for long wavelengths as R_{inj} is increased, and towards the upper wall at shorter wavelengths as R_{inj} is increased.

REFERENCES

Baines, P. G., Majumdar, S. J. & Mitsudera, H. 1996 The mechanics of the Tollmien–Schlichting wave. *J. Fluid Mech.* **312**, 107–124.

Berkowitz, B. 2002 Characterizing flow and transport in fractured geological media: a review. *Adv. Water Resour.* **25**, 861–884.

Chapman, S. J. 2002 Subcritical transition in channel flows. *J. Fluid Mech.* **451**, 35–97.

Cowley, S. J. & Smith, F. T. 1985. On the stability of Poiseuille–Couette flow: a bifurcation from infinity. *J. Fluid Mech.* **156**, 83–100.

Eckhardt, B., Schneider, T., Hof, B. & Westerweel, J. 1998 Turbulence transition in pipe flow. *Annu. Rev. Fluid Mech.* **39**, 447–468.

Faisst, H. & Eckhardt, B. 2003 Travelling waves in pipe flow. *Phys. Rev. Lett.* **91**, 224–502.

Fransson, J. & Alfredsson, P. 2003 On the hydrodynamic stability of channel flow with crossflow. *Phys. Fluids* **15**, 436–441.

Goharzadeh, A., Khalili, A. & Jrgensen, B. B. 2005 Transition layer thickness at a fluid–porous interface. *Phys. Fluids* **17**, 057102.

Hains, F. D. 1967 Stability of plane Couette–Poiseuille flow. *Phys. Fluids* **10**, 2079–2080.

Hains, F. D. 1971 Stability of plane Couette–Poiseuille flow with uniform crossflow. *Phys. Fluids* **14**, 1620–1623.

Hamilton, J. M., Kim, J. & Waleffe, F. 1995 Regeneration mechanism of near-wall turbulence structures. *J. Fluid Mech.* **287**, 317–348.

Hof, B., vanDoorne, C. W. H., Westerweel, J. & Nieuwstadt, F. T. M. 2005 Turbulence regeneration in pipe flow at moderate Reynolds numbers. *Phys. Rev. Lett.* **95**, 214502.

Hof, B., vanDoorne, C. W. H., Westerweel, J., Nieuwstadt, F. T. M., Faisst, H., Eckhardt, B., Wedin, H., Kerswell, R. R. & Waleffe, F. 2004 Experimental observation of nonlinear travelling waves in turbulent pipe flow. *Science* **305**, 1594–1598.

Joseph, D. D. 1968 Eigenvalue bounds for the Orr–Sommerfeld equation. *J. Fluid Mech.* **33**, 617–621.

Joseph, D. D. 1969 Eigenvalue bounds for the Orr–Sommerfeld equation. Part 2. *J. Fluid Mech.* **36**, 721–734.

Joslin, R. D. 1998 Aircraft laminar flow control. *Annu. Rev. Fluid Mech.* **30**, 1–29.

Kerswell, R. R. & Tutty, O. R. 2007 Recurrence of travelling waves in transitional pipe flow. *J. Fluid Mech.* **584**, 69–102.

Mack, L. M. 1976 A numerical study of the temporal eigenvalue spectrum of the Blasius boundary layer. *J. Fluid Mech.* **73**, 497–520.

Majdalani, J., Zhou, C. & Dawson, C. A. 2002 Two-dimensional viscous flow between slowly expanding or contracting walls with weak permeability. *J. Biomech.* **35**, 1399–1403.

Mott, J. E. & Joseph, D. D. 1968 Stability of parallel flow between concentric cylinders. *Phys. Fluids* **11**, 2065–2073.

Nicoud, F. & Angilella, J. R. 1997 Effects of uniform injection at the wall on the stability of Couette-like flows. *Phys. Rev.* E **56**, 3000–3009.

Orszag, S. A. 1971 Accurate solution of the Orr–Sommerfeld stability equation. *J. Fluid Mech.* **50**, 689–703.

Peixinho, J. & Mullin, T. 2006 Decay of turbulence in pipe flow. *Phys. Rev. Lett.* **96**, 094501.

Pfenniger, W. 1961 Transition in the inlet length of tubes at high Reynolds numbers. In *Boundary Layer and Flow Control* (ed. G. V. Lachman), pp. 970–980. Pergamon.

Potter, M. C. 1966 Stability of plane Couette–Poiseuille flow. *J. Fluid Mech* **24**, 609–619.

Reddy, S. C., Schmid, P. J. & Henningson, D. S. 1993 Pseudospectra of the Orr–Sommerfeld operator. *SIAM J. Appl. Maths* **53**, 15–47.

Reynolds, W. C. & Potter, M. C. 1967 Finite-amplitude instability of parallel shear flows. *J. Fluid Mech.* **27**, 465–492.

Romanov, V. A. 1973 Stability of plane parallel Couette flow. *Funct. Anal. Appl.* **7**, 137–146.

Sadeghi, V. M. & Higgins, B. G. 1991 Stability of sliding Couette–Poiseuille flow in an annulus subject to axisymmetric and asymmetric disturbances. *Phys. Fluids* A **3**, 2092–2104.

Sandblom, R. M. 2001 Filtering process. US Patent 4105547.

Schmid, P. J. 2007 Nonmodal stability theory. *Annu. Rev. Fluid Mech.* **39**, 129–162.

Schmid, P. J. & Henningson, D. S. 2001 *Stability and Transition in Shear Flows.* Springer.

Sheppard, D. M. 1972 Hydrodynamic stability of the flow between parallel porous walls. *Phys. Fluids* **15**, 241–244.

Squire, H. B. 1933 On the stability of three-dimensional disturbances of viscous flow between parallel walls. *Proc. R. Soc.* A **142**, 621–628.

Vadi, P. K. & Rizvi, S. S. H. 2001 Experimental evaluation of a uniform transmembrane pressure crossflow microfiltration unit for the concentration of micellar casein from skim milk. *J. Membr. Sci.* **189**, 69–82.

Waleffe, F. 1997 On a self-sustaining mechanism in shear flows. *Phys. Fluids* **9**, 883–900.

Wedin, H. & Kerswell, R. R. 2004 Exact coherent solutions in pipe flow: travelling wave solutions. *J. Fluid Mech.* **508**, 333–371.